



LJMU Research Online

Sharma, Y, Sollerman, J, Fremling, C, Kulkarni, SR, De, K, Irani, I, Schulze, S, Strotjohann, NL, Gal-Yam, A, Maguire, K, Perley, DA, Bellm, EC, Kool, EC, Brink, TG, Bruch, R, Deckers, M, Dekany, R, Dugas, A, Filippenko, AV, Goldwasser, S, Graham, MJ, Graham, ML, Groom, SL, Hankins, M, Jencson, J, Johansson, JP, Karambelkar, V, Kasliwal, MM, Masci, FJ, Medford, MS, Neill, JD, Nir, G, Riddle, RL, Rigault, M, Schweyer, T, Terwel, JH, Yan, L, Yang, Y and Yao, Y

A Systematic Study of Ia-CSM Supernovae from the ZTF Bright Transient Survey

<http://researchonline.ljmu.ac.uk/id/eprint/19965/>

Article

Citation (please note it is advisable to refer to the publisher's version if you intend to cite from this work)

Sharma, Y, Sollerman, J, Fremling, C, Kulkarni, SR, De, K, Irani, I, Schulze, S, Strotjohann, NL, Gal-Yam, A, Maguire, K, Perley, DA, Bellm, EC, Kool, EC, Brink, TG, Bruch, R, Deckers, M, Dekany, R, Dugas, A, Filippenko, AV, Goldwasser, S, Graham, MJ, Graham, ML, Groom, SL, Hankins, M, Jencson.

LJMU has developed [LJMU Research Online](http://researchonline.ljmu.ac.uk/) for users to access the research output of the University more effectively. Copyright © and Moral Rights for the papers on this site are retained by the individual authors and/or other copyright owners. Users may download and/or print one copy of any article(s) in LJMU Research Online to facilitate their private study or for non-commercial research. You may not engage in further distribution of the material or use it for any profit-making activities or any commercial gain.

The version presented here may differ from the published version or from the version of the record. Please see the repository URL above for details on accessing the published version and note that access may require a subscription.

<http://researchonline.ljmu.ac.uk/>

For more information please contact researchonline@ljmu.ac.uk

<http://researchonline.ljmu.ac.uk/>



A Systematic Study of Ia-CSM Supernovae from the ZTF Bright Transient Survey

Yashvi Sharma¹, Jesper Sollerman², Christoffer Fremling¹, Shrinivas R. Kulkarni¹, Kishalay De³, Ido Irani⁴, Steve Schulze⁵, Nora Linn Strotjohann⁴, Avishay Gal-Yam⁴, Kate Maguire⁶, Daniel A. Perley⁷, Eric C. Bellm⁸, Erik C. Kool², Thomas G. Brink⁹, Rachel Bruch⁴, Maxime Deckers⁶, Richard Dekany¹⁰, Alison Dugas¹¹, Alexei V. Filippenko⁹, Samantha Goldwasser⁴, Matthew J. Graham¹, Melissa L. Graham⁸, Steven L. Groom¹², Matt Hankins¹³, Jacob Jencson¹⁴, Joel P. Johansson⁵, Viraj Karambelkar¹, Mansi M. Kasliwal¹, Frank J. Masci¹², Michael S. Medford^{15,16}, James D. Neill¹, Guy Nir⁹, Reed L. Riddle¹⁰, Mickael Rigault¹⁷, Tassilo Schweyer², Jacco H. Terwel^{6,18}, Lin Yan¹, Yi Yang (杨轶)⁹, and Yuhao Yao¹

¹ Division of Physics, Mathematics and Astronomy, California Institute of Technology, Pasadena, CA, 91125, USA; yssharma@astro.caltech.edu

² Department of Astronomy, The Oskar Klein Center, Stockholm University, AlbaNova, SE-10691 Stockholm, Sweden

³ MIT-Kavli Institute for Astrophysics and Space Research, Cambridge, MA, 02139, USA

⁴ Department of Particle Physics and Astrophysics, Weizmann Institute of Science, 234 Herzl Street, 76100 Rehovot, Israel

⁵ Department of Physics, The Oskar Klein Center, Stockholm University, AlbaNova, SE-10691 Stockholm, Sweden

⁶ School of Physics, Trinity College Dublin, the University of Dublin, College Green, Dublin, Ireland

⁷ Astrophysics Research Institute, Liverpool John Moores University, Liverpool Science Park, 146 Brownlow Hill, Liverpool, L3 5RF, UK

⁸ DIRAC Institute, Department of Astronomy, University of Washington, 3910 15th Avenue NE, Seattle, WA, 98195, USA

⁹ Department of Astronomy, University of California, Berkeley, CA, 94720-3411, USA

¹⁰ Caltech Optical Observatories, California Institute of Technology, Pasadena, CA, 91125, USA

¹¹ Institute for Astronomy, University of Hawai'i, Honolulu, HI, 96822, USA

¹² IPAC, California Institute of Technology, 1200 E. California Boulevard, Pasadena, CA, 91125, USA

¹³ Arkansas Tech University, Russellville, AR, 72801, USA

¹⁴ Steward Observatory, University of Arizona, 933 North Cherry Avenue, Tucson, AZ, 85721-0065, USA

¹⁵ Department of Astronomy, University of California, Berkeley, Berkeley, CA, 94720, USA

¹⁶ Lawrence Berkeley National Laboratory, 1 Cyclotron Road, Berkeley, CA, 94720, USA

¹⁷ Université Clermont Auvergne, CNRS/IN2P3, Laboratoire de Physique de Clermont, F-63000 Clermont-Ferrand, France

¹⁸ Isaac Newton Group (ING), Apt. de correos 321, E-38700, Santa Cruz de La Palma, Canary Islands, Spain

Received 2022 October 11; revised 2023 February 7; accepted 2023 February 13; published 2023 May 5

Abstract

Among the supernovae (SNe) that show strong interaction with a circumstellar medium (CSM), there is a rare subclass of Type Ia supernovae, SNe Ia-CSM, which show strong narrow hydrogen emission lines much like SNe IIn but on top of a diluted Type Ia spectrum. The only previous systematic study of this class identified 16 SNe Ia-CSM, eight historic and eight from the Palomar Transient Factory (PTF). Now using the successor survey to PTF, the Zwicky Transient Facility (ZTF), we have classified 12 additional SNe Ia-CSM through the systematic Bright Transient Survey (BTS). Consistent with previous studies, we find these SNe to have slowly evolving optical light curves with peak absolute magnitudes between -19.1 and -21 , spectra having weak $H\beta$ and large Balmer decrements of ~ 7 . Out of the 10 SNe from our sample observed by NEOWISE, nine have 3σ detections, with some SNe showing a reduction in the red wing of $H\alpha$, indicative of newly formed dust. We do not find our SN Ia-CSM sample to have a significantly different distribution of equivalent widths of He I $\lambda 5876$ than SNe IIn as observed in Silverman et al. The hosts tend to be late-type galaxies with recent star formation. We derive a rate estimate of $29^{+27}_{-21} \text{ Gpc}^{-3} \text{ yr}^{-1}$ for SNe Ia-CSM, which is $\sim 0.02\%$ – 0.2% of the SN Ia rate. We also identify six ambiguous SNe IIn/Ia-CSM in the BTS sample and including them gives an upper limit rate of 0.07% – 0.8% . This work nearly doubles the sample of well-studied Ia-CSM objects in Silverman et al., increasing the total number to 28.

Unified Astronomy Thesaurus concepts: [Supernovae \(1668\)](#); [Type Ia supernovae \(1728\)](#)

1. Introduction

When it comes to supernovae (SNe) interacting with a circumstellar medium (CSM), a number of subtypes of core-collapse SNe (CCSNe) show signs of strong interaction, like SNe IIn (Schlegel 1990; Filippenko 1997), SNe Ibn (Foley et al. 2007; Pastorello et al. 2008; Chugai 2009; Hosseinzadeh et al. 2017), and most recently SNe Icn (Gal-Yam et al. 2021, 2022; Perley et al. 2022). SN IIn progenitors are generally thought to be massive stars (like luminous blue variables, LBVs) that lose their hydrogen envelopes to wind-

driven mass loss and outbursts (Gal-Yam et al. 2007; Gal-Yam & Leonard 2009; Kiewe et al. 2012; Taddia et al. 2013; Smith 2014). Helium-rich but hydrogen-deficient CSM in the case of SNe Ibn (Foley et al. 2007; Pastorello et al. 2008; Chugai 2009) and both hydrogen- and helium-deficient CSM in SNe Icn (Gal-Yam et al. 2022; Pellegrino et al. 2022; Perley et al. 2022) are thought to arise from high-velocity wind mass loss or stripping of the envelope in binary configurations of massive Wolf-Rayet (W-R)-like stars. For SNe IIn in most cases, the mass-loss rate derived from the CSM velocity is consistent with estimates from LBV-like eruptive mass loss.

However, there exists a rare subtype of thermonuclear SN (SNe Ia) which also interacts strongly with a CSM i.e., SNe Ia-CSM. This class poses a challenge to the progenitor debate of SNe Ia. There is some consensus on there being at least two



Original content from this work may be used under the terms of the [Creative Commons Attribution 4.0 licence](#). Any further distribution of this work must maintain attribution to the author(s) and the title of the work, journal citation and DOI.

major progenitor channels for SNe Ia: the double-degenerate (DD) channel (Iben & Tutukov 1984; Webbink 1984), which is the merging of two CO white dwarfs (WDs), and the single-degenerate (SD) channel (Whelan & Iben 1973), where the WD accretes enough material from a nondegenerate companion to explode. Although there are more arguments for the DD scenario from observations of nearby SNe Ia (Bloom et al. 2011; Li et al. 2011; Nugent et al. 2011; Brown et al. 2012), the strongest observational evidence for the SD scenario are SNe Ia with a CSM.

Indications of CSM around SNe Ia range from the detection of time-varying narrow Na I D absorption lines (Patat et al. 2007; Blondin et al. 2009; Simon et al. 2009) in high-resolution spectra (found in at least 20% of SNe Ia in spiral hosts; Sternberg et al. 2011; Maguire et al. 2013; Clark et al. 2021), to strong, intermediate, and narrow Balmer emission features in the spectra, and large deviations of the light curves from the standard shape. The latter phenomena have been named SNe Ia-CSM (Silverman et al. 2013), but were earlier referred to as “SNe IIna” or “SNe IIn” due to the strong similarity between their spectra and those of SNe IIn. The first two examples of this class studied in detail were SNe 2002ic (Hamuy et al. 2003; Chugai et al. 2004; Deng et al. 2004; Wang et al. 2004; Wood-Vasey et al. 2004; Kotak & Meikle 2005) and 2005gj (Aldering et al. 2006; Prieto et al. 2007), but for a long time there was ambiguity regarding their thermonuclear nature (Benetti et al. 2006). These SNe were dominated by interaction from the first spectrum and were quite overluminous compared to normal SNe Ia. The first clear example of a thermonuclear SN Ia-CSM was PTF11kx (Dilday et al. 2012; Silverman et al. 2013). It looked like a luminous SN Ia (99aa-like; Filippenko et al. 1999) at early phases but started showing interaction at ~ 60 days from explosion and thereafter strongly resembled SNe 2002ic and 2005gj at late times. Higher-resolution spectra taken at early times indicated multiple shells of CSM with some evacuated regions in between. Dilday et al. (2012) suggested a symbiotic nova progenitor involving a WD and a red giant (similar to RS Ophiuchi) could produce such a CSM distribution; however, later studies argued that the massive CSM of PTF11kx was inconsistent with the mass-loss rates from symbiotic nova systems (Silverman et al. 2013; Soker et al. 2013).

Ever since, a handful of SNe of this class have been studied in detail to investigate their progenitors and to distinguish them from their spectroscopic cousins, Type IIn SNe. Both SN Ia-CSM and SN IIn spectra share a blue quasi-continuum, a strong $H\alpha$ feature with an intermediate and a narrow component, and often a broad Ca near-infrared (NIR) triplet feature, but they differ with regards to the line strength of $H\beta$, the strength/presence of helium, and the presence of emission lines from intermediate mass elements often found in CCSNe. There are some individual SNe with an unclear type often referred to as SN Ia-CSM/IIn, like SN 2012ca for which some papers argue for a CC origin (Inserra et al. 2014, 2016) and others for a thermonuclear origin (Fox et al. 2015). This ambiguity becomes more dominant as the underlying SN flux gets dimmer compared to the interaction power (Leloudas et al. 2015). Silverman et al. (2013; hereafter S13) is the only study to analyse a sample of SNe Ia-CSM, 16 objects in total including six previously known, three rediscovered (reclassified SNe IIn), and seven new from the Palomar Transient Factory (PTF). Their paper presents the common properties of

the optical light curves, spectra, and host galaxies and contrast them against SN IIn properties. In this paper, we present 12 new SNe Ia-CSM discovered as part of the Zwicky Transient Facility’s (ZTF; Bellm et al. 2019; Graham et al. 2019; Dekany et al. 2020) Bright Transient Survey (BTS; Fremling et al. 2020; Perley et al. 2020) and analyse their optical light curves, spectra, hosts, and rates. Throughout this paper, we have compared the results derived from our sample to the ones in S13.

This paper is organized as follows; we first discuss the sample selection criteria, the photometric and spectroscopic data collection in Section 2, then an analysis of the light curves and color curves and the bolometric luminosities is done in Section 3.1. An analysis of early- and late-time spectra and emission-line identification is presented in Section 3.2, and an analysis of the host galaxies is provided in Section 3.3. The rates are estimated from the BTS survey in Section 3.4. We end with a discussion about the nature of SN Ia-CSM progenitors and a summary in Sections 4 and 5, respectively.

2. Observations and Data Reduction

In this section, we outline our selection criteria, and present the optical photometry and spectroscopic observations of the 12 SNe Ia-CSM in our sample.

2.1. Selection Criteria

To curate our sample of SNe Ia-CSM carefully, we used the BTS sample and its publicly available BTS Sample Explorer¹⁹ website to obtain a list of all classified Type Ia subtypes during the period 2018 May 1 to 2021 May 1. We then filter out oddly behaving Type Ia SNe based on their light-curve properties. We used two criteria: the primary being the rest-frame duration by considering the flux above 20% of the peak flux, and the second being the change in magnitude after 30 days from peak (Δm_{30}). We calculated these two properties from either g - or r -band light curves (whichever had the maximum number of detections) grouped into 3 day bins and used Gaussian process regression²⁰ to interpolate the light curves where coverage was missing. For the first filtering, we calculated the mean ($\mu \approx 35$ days) and standard deviation ($\sigma \approx 16$ days) of the duration distribution and selected everything that had a duration greater than $\mu + 3\sigma$. Given the large sample size ($N = 3486$), the standard error on the mean is ~ 0.5 day, hence our duration cut of 3σ is suitable. This filtering selected 41 out of 3486 BTS SNe Ia. Then from these 41 SNe, we calculated the mean and standard deviation of the Δm_{30} distribution and removed SNe that were more than 1σ away from the mean on the higher side to reject the relatively steeply declining long SNe, which resulted in 35 SNe being kept. Again, the mean and standard deviation of Δm_{30} distribution of these 41 long-duration SNe are 0.48 mag and 0.27 mag, respectively, and the standard error on mean is ~ 0.04 , making our 1σ cut suitable. Finally, we manually inspected the 35 selected SNe Ia to confirm their classification. 20 out of the 35 SNe that passed the above filtering criteria were just normal SNe Ia either caught late or missing some postpeak coverage in ZTF or had spurious detections that resulted in long-duration estimates, two had incorrect duration estimates due to interpolation errors and

¹⁹ <https://sites.astro.caltech.edu/ztf/bts/explorer.php>

²⁰ Pedregosa et al. (2011) https://scikit-learn.org/stable/modules/gaussian_process.html.

Table 1
Properties of the 12 BTS SNe Ia-CSM

ZTF Name	IAU Name	z	M_r^{peak} (mag)	Duration ^a (days)	Host Name	Host Mag ^b (m_r)
ZTF18aaykjei	SN 2018crl	0.097	−19.66	130	SDSS J161938.90 + 491104.5	18.89
ZTF18abuafp	SN 2018gkx	0.1366	−20.07	322	SDSS J135219.22 + 553830.2	18.23
ZTF18actuhrs	SN 2018evt	0.02378	−19.10	447	MCG-01-35-011	14.07
ZTF19aaeoqst	SN 2019agi	0.0594	<−18.76	>303	SDSS J162244.06 + 240113.4	17.82
ZTF19abidbqp	SN 2019ibk	0.04016	<−17.55	>576	SDSS J014611.93−161701.1	15.55
ZTF19acbiddp	SN 2019rvb	0.1835	−20.74	172	WISEA J163809.90 + 682746.3	20.44
ZTF20abmlrx	SN 2020onv	0.095	<−20.36	>154	WISEA J231646.31−231839.9	17.95
ZTF20abqkbfx	SN 2020qzx	0.0964	−20.00	166	WISEA J180400.99 + 740050.0	17.65
ZTF20accmutv	SN 2020uem	0.041	<−20.17	>279	WISEA J082423.32−032918.6	15.88
ZTF20aciwcuz	SN 2020xtg	0.0612	<−19.60	>336	SDSS J153317.64 + 450022.8	15.42
ZTF20acqikeh	SN 2020abfe	0.093	−20.24	171	SDSS J200003.30 + 100904.2	20.18
ZTF21aaabwzx	SN 2020aekp	0.046	−19.62	458	SDSS J154311.45 + 174843.7	18.41

Notes.

^a Rest-frame duration above 20% of the peak r -band flux, uncertainty of ± 2 –3 days from ZTF cadence.

^b Corrected for Galactic extinction.

were recalculated, and one (AT2020caa; Soraisam et al. 2021) had some detections before the SN explosion which could be connected to a different SN (i.e., a sibling; Graham et al. 2022).

The remaining 12 long-duration SNe Ia all turned out to be spectroscopically classified SNe Ia-CSM in BTS, and none of the classified BTS SNe Ia-CSM were missed in this filtering. No other SNe apart from these stood out in particular, indicating the classification reliability of the BTS sample. During the same period, nine SNe Ia-CSM were reported to the Transient Name Server (TNS), out of which seven are already in our sample, one was detected by ZTF but did not meet the BTS criteria, and one was not detected by ZTF as the transient location fell too close to the field edges and was masked by the automated image subtraction pipeline. Yao et al. (2019) presented early photometric observations of one SN Ia-CSM in our sample, SN 2018crl. Table 1 summarizes the coordinates, redshifts, peak absolute magnitudes, durations, host galaxy information, and Milky Way extinction for the 12 SNe Ia-CSM in our sample.

Furthermore, we rechecked the classifications of 142 SNe II in classified in BTS during the same period as above, in case any SNe Ia-CSM were masquerading among them and found six to have ambiguous classifications. These are discussed further in the Appendix.

2.2. Discovery

All SNe Ia-CSM were detected by ZTF (Bellm et al. 2019; Graham et al. 2019; Dekany et al. 2020) and passed the criteria for BTS’s (Fremling et al. 2020; Perley et al. 2020) automatic filtering, i.e., extragalactic real transients with peak magnitudes brighter than 19 mag. These were saved and classified as part of BTS, which aims to classify all transients brighter than 18.5 mag, and reported to the TNS²¹ during the period 2018 May 1 to 2021 May 1. Out of the 12 SNe, six were first reported to TNS (i.e., discovered) by ZTF (AMPEL; Soumagnac & Ofek 2018; Nordin et al. 2019; BTS), three were first reported by GaiaAlerts (Hodgkin et al. 2021), two by ATLAS (Smith et al. 2020), and one by ASAS-SN (Shappee et al. 2014). For classification, nine were classified by the ZTF group, one by

ePESTO (Smartt et al. 2015; Stein et al. 2018), one by SCAT (Tucker et al. 2018; Payne et al. 2019), and one by the Trinity College Dublin (TCD) group (Prentice et al. 2020). Follow-up spectral series for these SNe were obtained as part of the BTS classification campaign as many were difficult to classify with the ultra low-resolution spectrograph P60/SEDM (Blagorodnova et al. 2018), and hence were followed up with intermediate-resolution spectrographs. The SEDM spectra were helpful in determining an initial redshift but the template matches were unclear (matched to SN II in as well as SN Ia-CSM and SN Ia-pec templates, some matched poorly to SN Ia/Ic at early times). SNe 2019agi (classification and spectrum taken from TNS), 2019rvb, 2020onv, 2020qzx, and 2020uem were classified as Ia-CSM ~ 1 –2 months after discovery using spectra at phases of 42, 26, 38, 45, and 51 days, respectively. SNe 2018crl, 2018gkx, and 2019ibk were classified ~ 2 –3 months after discovery using spectra at phases of 92, 75, and 103 days, respectively. SNe 2018evt, 2020abfe, and 2020aekp were classified ~ 4 –5 months after discovery using spectra at phases of 144, 146, and 132 days, respectively. SN 2020xtg immediately went behind the Sun after its first detection by ZTF; therefore, its first spectrum (using SEDM) was taken at 91 days since explosion, which was dominated by strong H α emission, and thus SN 2020xtg was initially classified as a Type II. As this SN was exhibiting a long-lasting light curve, an intermediate-resolution spectrum was taken at 340 days which matched very well to SNe Ia-CSM and therefore its classification was updated. SNe 2020uem and 2020aekp showed peculiar features and were followed up for more optical spectroscopy for single-object studies (C. Cold et al. 2023, in preparation).

2.3. Optical Photometry

To assemble our sample light curves, we obtained forced point-spread function (PSF) photometry via the ZTF forced-photometry service (Masci et al. 2019; IRSA 2022) in the g , r , and i bands and also added data from ATLAS’s (Tonry et al. 2018; Smith et al. 2020) forced-photometry service in the c and o bands. The high-cadence ZTF partnership survey in the i band contributed some photometry to SNe 2018crl, 2018gkx, 2019agi, 2019ibk, and 2019rvb. The ZTF and ATLAS data were supplemented with data from the Rainbow camera

²¹ <https://www.wis-tns.org/>

(RC; Ben-Ami et al. 2012) on the robotic Palomar 60 inch telescope (P60; Cenko et al. 2006) and the optical wide-field camera (IO:O) on the Liverpool telescope (LT; Steele et al. 2004). The P60 data were processed with the automatic image subtraction pipeline `FPipe` (Fremling et al. 2016) using reference images from the Sloan Digital Sky Survey (SDSS) when available, and otherwise from the Panoramic Survey Telescope and Rapid Response System (Pan-STARRS). The IO:O data were initially reduced with their standard pipeline²² then image subtraction was carried out using the method outlined in Taggart (2020). For SN 2018evt, some early-time data available from ASAS-SN (Shappee et al. 2014; Kochanek et al. 2017) in the V band were obtained through their *Sky Patrol*²³ interface.

We corrected all photometry for Milky Way extinction with the Python package `extinction` (Barbary 2016) using the dust extinction function from Fitzpatrick (1999), the Schlafly & Finkbeiner (2011) dust map, and an R_V of 3.1. Then we converted all measurements into flux units for analysis and considered anything less than a 3σ detection an upper limit. There is moderate to good coverage in the g , r , c , and o bands for all SNe in our sample. Figure 1 shows a multipaneled figure of the light curves of the objects in our sample.

2.4. Mid-IR Photometry

The transients were observed during the ongoing NEOWISE all-sky mid-IR survey in the W1 ($3.4\ \mu\text{m}$) and W2 ($4.5\ \mu\text{m}$) bands (Wright et al. 2010; Mainzer et al. 2014). We retrieved time-resolved coadded images of the fields created as part of the unWISE project (Lang 2014a; Meisner et al. 2018). To remove contamination from the host galaxies, we used a custom code (De et al. 2020) based on the ZOGY algorithm (Zackay et al. 2016) to perform image subtraction on the NEOWISE images using the full-depth coadds of the WISE and NEOWISE mission (obtained during 2010–2014) as reference images. Photometric measurements were obtained by performing forced PSF photometry at the transient positions in the subtracted WISE images until the epoch of the last NEOWISE data release (data acquired until 2021 December). Further analysis of the mid-IR photometry is presented in Section 3.1.4.

2.5. Optical Spectroscopy

The main instruments used for taking spectra and the software used to reduce the data are summarized in Table 2. Additionally, the spectrum Reguitti (2020) obtained using the Asiago Faint Object Spectrograph and Camera (AFOSC) on the 1.8 m telescope at Cima Ekar, and the spectrum Stein et al. (2018) obtained using the ESO Faint Object Spectrograph and Camera version 2 (EFOC2) on ESO’s New Technology Telescope (NTT) were taken from TNS.

The details for all optical spectra (61 for the sample in total) presented in this paper are provided in Table 3. Furthermore, all spectra were corrected for Milky Way extinction using `extinction` and the same procedure as for the photometry. The SN redshifts were derived using narrow host lines for objects which did not already have a host redshift available in the NASA/IPAC Extragalactic Database²⁴ (NED). Photometric calibration was done for all spectra i.e., they were scaled such

that the synthetic photometry from the spectrum matched the contemporaneous host-subtracted ZTF r -band data. For SN 2018crl, a host galaxy spectrum taken using P200/DBSP was available, which was subtracted from the P200/DBSP SN spectrum taken at +92 days. For SN 2020aekp, more spectra beyond ~ 350 days were obtained but will be presented in Cold et al. 2023, (in preparation; 34 additional spectra up to ~ 600 days).

These processed spectra were used for the rest of the analysis as detailed in Section 3.2 and will be available on WISeREP²⁵ (Yaron & Gal-Yam 2012).

3. Analysis

3.1. Photometry

3.1.1. Explosion Epoch Estimates

For the purpose of this paper, the “explosion time” simply refers to the time when the optical flux rises above the zero-point baseline (i.e., first light). We used prepeak g -, r -, and i -band ZTF photometry and c - and o -band ATLAS photometry (binned in 1 day bins), when available, for our analysis. For each SN, the light curve was interpolated using Gaussian process regression to obtain the peak-flux epoch, then a power-law (PL) model was fit using epochs from baseline to 60% of the peak brightness in each band following Miller et al. (2020). The PL fits converged in at least one band for six out of the 12 BTS SNe Ia-CSM. For the rest, we simply took the middle point between the first 5σ detection and the last upper limit before this detection as the explosion epoch with half of the separation between these two points as the uncertainty.

The explosion time estimates, light-curve bands used for the PL fits, and the 1σ uncertainties of the explosion times are listed in Table 4. The unfilled “PL fit filters” column in the table show the SNe for which the PL fit did not converge, and averages were instead used. For the PL fits this typically constrains the time of explosion to within a fraction of a day. Given the high cadence of the ZTF survey, even in the cases where we use only the last nondetection, the uncertainty range is typically less than 3 days. Only for SN 2020uem is the date of explosion virtually unconstrained (± 57 days) as it was behind the Sun at the time of explosion.

Although for SN 2019ibk the explosion time is formally constrained with a ± 3 day uncertainty, this estimate was derived using only ATLAS o -band data right after the SN emerged from behind the Sun. There is not a clear rise observed over a few epochs but two nondetections before a 5σ detection. It is possible that the actual peak of this SN occurred earlier while it was behind the Sun and the rising o -band points after it emerged are due to a second peak or bump (similar to SN 2018evt; in that case, the actual rise was caught before the SN went behind the Sun in the ASAS-SN data). If the former explosion epoch estimate from the o -band data is to be believed then SN 2019ibk would be the most subluminous among the SNe Ia-CSM, peaking at -17.5 .

3.1.2. Duration and Absolute Magnitudes

Figure 2 shows the SNe Ia-CSM (colored squares) in our sample in the duration–luminosity and duration– Δm_{30} phase spaces. In the top panel, the x -axis is the duration above half-

²² <https://telescope.livjm.ac.uk/TelInst/Pipelines/>

²³ <https://asas-sn.osu.edu/>

²⁴ <https://ned.ipac.caltech.edu/>

²⁵ <https://www.wiserep.org/>

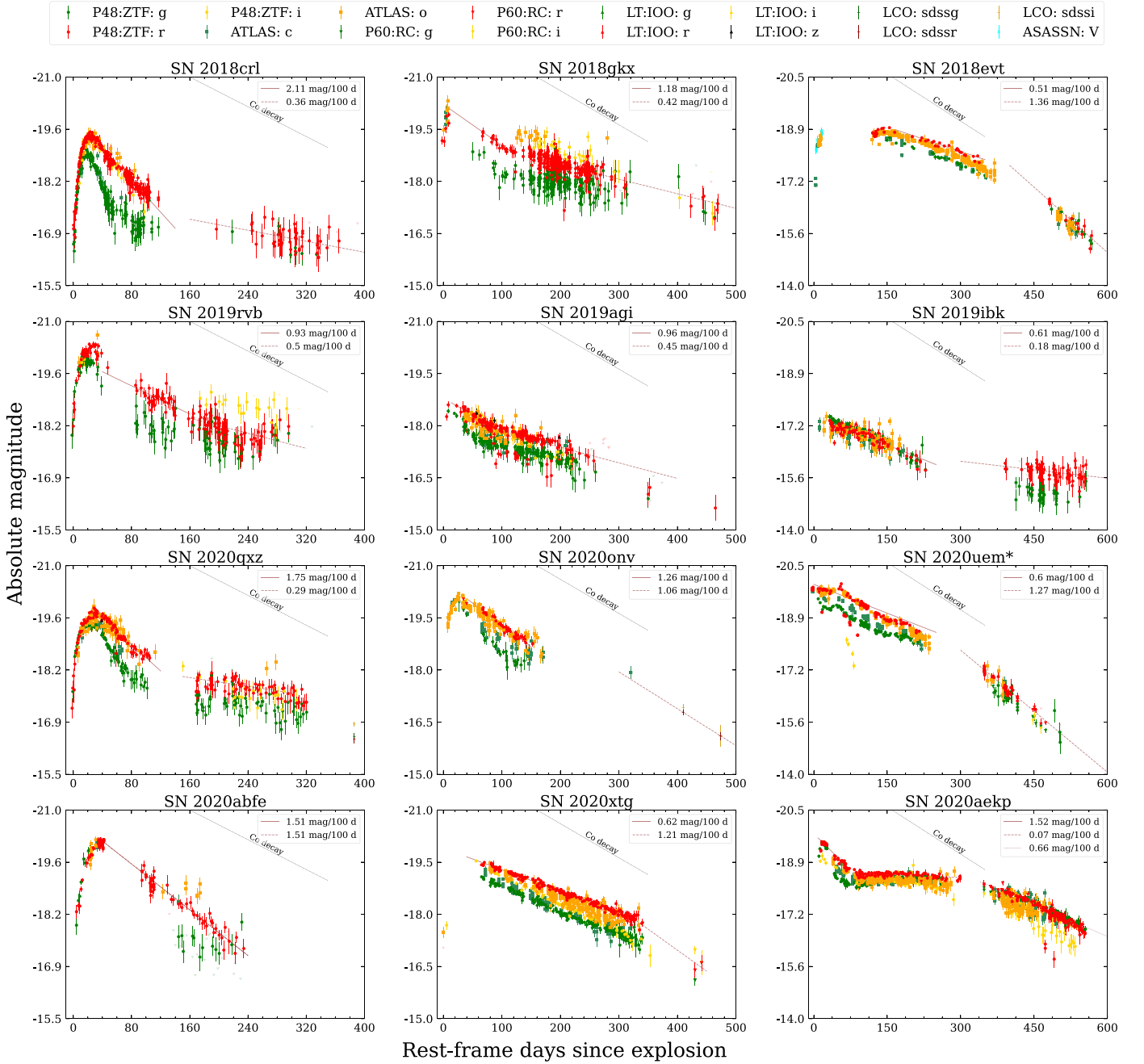


Figure 1. Optical light curves of the ZTF BTS SN Ia-CSM sample. The SNe Ia-CSM have longer durations than the average SN Ia, with some variety like bumpy light curves or long plateaus. The one SN marked with an asterisk (SN 2020uem) has an unconstrained explosion time estimate ($\sim \pm 50$ days). The decline rate from cobalt decay is marked with a black dashed line. The light-curve decline rates measured from the r -band data are shown in the subplot legends.

max and the y -axis is the peak absolute magnitude (see Table 1) when we have photometric coverage both prepeak and postpeak. For SNe missing prepeak coverage, their discovery magnitudes are taken to be an upper limit to their peak absolute magnitudes and the duration from discovery a lower limit to the duration above half-max (marked by arrows in Figure 2). The BTS SN Ia sample is shown in gray points, and we also show the SNe Ia-CSM presented in S13 with empty triangles for comparison in the top panel. In the bottom panel, the x -axis is the duration above 20% of the peak flux (Δt_{20}) and the y -axis is Δm_{30} , the two parameters used in the selection criteria. Most of the SNe Ia-CSM lie on the longer-duration and brighter-

luminosity side, and are even more distinctly separated in the Δt_{20} - Δm_{30} phase space. This makes the SN initial decline rate and duration useful tools for identifying thermonuclear SNe potentially interacting with a CSM, if they have not revealed themselves already in their early-time spectra. The gray points lying in the same phase space as SNe Ia-CSM are the false-positive cases described in Section 2.1. Also worth noting is that the duration calculated by taking the flux above half of the peak-flux value does not capture the true duration of the light curve when the plateau phase falls below half-max, as is the case for SN 2020aekp (>500 day light curve) but Δt_{20} and Δm_{30} do.

Table 2

Description of the Spectrographs Used for Follow up and the Corresponding Data Reduction Pipelines

Inst.	Telescope	Reduction Software
SEDM ^a	Palomar 60 inch (P60)	pySEDM ^b
ALFOSC ^c	Nordic Optical Telescope	IRAF ^d , PyNOT ⁿ , pypeit
DBSP ^e	Palomar 200 inch (P200)	IRAF ^f , DBSP_DRP ^g
KAST ^h	Shane 3 m	IRAF
LRIS ⁱ	Keck I	LPipe ^j
SPRAT ^k	Liverpool Telescope	Barnsley et al. (2012)
DIS ^l	APO ^m	IRAF

Notes.^a Spectral Energy Distribution Machine (Blagorodnova et al. 2018).^b Rigault et al. (2019).^c Andalusia Faint Object Spectrograph and Camera.^d Tody (1986, 1993).^e Double Beam Spectrograph (Oke & Gunn 1982).^f Standard pipeline by Bellm & Sesar (2016) used prior to fall 2020.^g pypeit (Prochaska et al. 2020)-based pipeline (https://github.com/finagle29/dbsp_drp) used since fall 2020.^h Kast Double Spectrograph (Miller & Stone 1987).ⁱ Low Resolution Imaging Spectrometer (Oke et al. 1995).^j IDL-based automatic reduction pipeline (<https://sites.astro.caltech.edu/~dperley/programs/lpipe.html>) (Perley 2019).^k Spectrograph for the Rapid Acquisition of Transients (Piascik et al. 2014).^l Dual Imaging Spectrograph.^m Astrophysics Research Consortium telescope at the Apache Point Observatory.ⁿ <https://github.com/jkrogager/PyNOT>.**3.1.3. Light and Color Curves**

We have good prepeak coverage of ZTF data for eight of the 12 SNe in our sample.²⁶ SN 2018evt was discovered by ASAS-SN on JD 2458341.91 (Nicholls & Dong 2018) and classified by ePESSTO the next day (Stein et al. 2018), around 115 days before the first detection by ZTF when the SN came back from behind the Sun. Hence we have only one epoch of prepeak photometry and one early spectrum for SN 2018evt.

Our mixed bag of SNe Ia-CSM show postmaximum decline rates ranging from 0.5 to 2.0 mag 100 day⁻¹ in the r band from peak to ~ 100 days postpeak. The median decline rate is 1.07 mag 100 day⁻¹, which is much slower than the decline rates of normal SNe Ia. We see a variety of changes in the decline rates after around 100 days from peak. Two SNe (2020onv and 2020abfe) show no change and have a constant slow decline throughout. Four SNe (2018gkx, 2019agi, 2019ibk, and 2019rvb) evolve to a shallower slope going from ~ 0.6 –1 mag 100 day⁻¹ to ~ 0.2 –0.5 mag 100 day⁻¹. Three SNe (2018crl, 2020qzx, and 2020aekp) show a major change in the decline rate with the light curves becoming almost flat, and SN 2020aekp shifts back to a slow decline from this plateau after ~ 200 days. In three cases, the decline rate actually becomes steeper: SN 2018evt goes from 0.52 mag 100 day⁻¹ to 1.4 mag 100 day⁻¹, SN 2020uem goes from 0.52 mag 100 day⁻¹ to 1.25 mag 100 day⁻¹, and SN 2020xtg seems to go from 0.61 mag 100 day⁻¹ to 1.35 mag 100 day⁻¹ (even though there is only one epoch at late times to measure this change). The three SNe with the fastest initial decline rates ($\gtrsim 1.5$ mag 100 day⁻¹ in the r band) are similar to SN 2002ic (initial decline of 1.66 mag 100 day⁻¹ in V) and PTF11kx (initial

decline of 3.3 mag 100 day⁻¹ in R), and coincidentally are also the ones that evolve into a plateau. The rest of the sample have initial decline rates comparable to SN 1997cy (0.75 mag 100 day⁻¹) and SN 2005gj (0.88 mag 100 day⁻¹) (Inserra et al. 2016). From these observations, we can conclude that SNe Ia-CSM exhibit a range of slow evolution indicating that there exists a continuum of phases at which strong CSM interaction begins to dominate the powering of the light curves for these SNe. It is, however, difficult to pinpoint the exact phase when interaction starts from the light curve without modeling. CSM interaction could be affecting the peak brightness significantly even in cases where interaction only appears to dominate after a few weeks (SNe 2018crl, 2020qzx, and 2020aekp). Considering the average peak phase to be ~ 20 days past explosion from the light curves and assuming an ejecta velocity of $\sim 20,000$ km s⁻¹, the CSM is located at $\sim 3.5 \times 10^{15}$ cm. This estimate can be refined by considering the phase of the earliest spectrum that shows interaction signatures (see Section 3.2). At late times, all the decline rates are slower than that expected from cobalt decay (0.98 mag 100 day⁻¹), confirming that the power from CSM interaction dominates the light-curve behavior for a long time.

Figure 3 shows the $g - r$ color evolution of our sample SNe as a function of phase (rest-frame days from r -band maximum), comparing them with some famous SNe Ia-CSM (SNe 2005gj, 1997cy, and 1999E), and SNe 2012ca (Ia-CSM/IIn), 2010jl (IIn), and 1991T (overluminous Type Ia). The color evolution of normal SNe Ia from ZTF (Dhawan et al. 2022) is shown in gray lines. We use $g - r$ colors when available, otherwise we estimate the $g - r$ color by fitting Planck functions to estimate the blackbody temperatures from the $V - R$ colors. Our SNe Ia-CSM show similar color evolution as the older Type Ia-CSM/IIn interacting SNe, i.e., the $g - r$ color increases gradually for about 100 days and then settles into a plateau or slowly declines, and one object (SN 2019ibk) becomes redder at late times similar to SN 2012ca. These interacting SNe are redder at late times compared to normal SNe Ia.

3.1.4. Mid-IR Brightness Comparison

Out of the 12 SNe in our sample, only one observed (SN 2020abfe) did not have 3σ detections post explosion in the unWISE difference photometry light curves and two (SNe 2019rvb and 2020qzx) did not have coverage post explosion. The unWISE light curves for the rest of the SNe Ia-CSM having $>3\sigma$ detections in the W1 (3.3 μ m) and W2 (4.6 μ m) bands are shown in Figure 4 (black and red stars) along with Spitzer IRAC survey data of SN 2008cg (indigo and magenta empty triangles) and SN 2008J (indigo and magenta empty squares) (both Ia-CSM), and some SNe IIn (blue and orange crosses) taken from Fox et al. (2011). The most nearby SN in our sample, SN 2018evt, is among the brightest (~ 17 AB mag) in the MIR at least until ~ 1000 days after explosion and it has a bumpy light curve. SNe 2019ibk and 2018crl however are the most luminous with an absolute magnitude of -18.7 mag in the W1 band. The brightness of the BTS SNe Ia-CSM are comparable with other interacting SNe and span a similar range (-16 to -19). However, SNe IIn have been detected until even later epochs (up to 1600 days) than SNe Ia-CSM, probably due to the larger number of SNe IIn at closer distances. SN 2020abfe has upper limits around ~ -18 in the W1 band and ~ -18.5 in the W2 band up to ~ 300 days post explosion, as shown with upside-down filled triangles. As the

²⁶ except for SNe 2018evt, 2019ibk, 2020onv, and 2020uem.

Table 3
Summary of the Optical Spectra

SN	JD (−2450000)	Epoch (days)	Telescope/Instrument	Int (s)	SN	JD (−2450000)	Epoch (days)	Tel./Instr.	Int (sec)
SN 2018crl	8282	9	APO/DIS	2400	SN 2020uem	9128	11	P60/SEDM	1800
	8288	15	P60/SEDM	2700		9136	18	P60/SEDM	1800
	8295	21	P60/SEDM	2700		9170	51	Ekar/AFOSC	1200
	8306	31	P60/SEDM	2700		9222	101	Lick-3 m/KAST	3600
	8373	92	P200/DBSP	600		9252	130	Lick-3 m/KAST	2700
(host)	8627	324	P200/DBSP	900		9263	140	Lick-3 m/KAST	2400
SN 2018gkx	8457	75	Keck I/LRIS	300		9291	167	NOT/ALFOSC	900
SN 2018evt	8343	9	NTT/EFOSC2	300		9481	349	P60/SEDM	2160
	8465	127	P60/SEDM	1200		9492	360	Keck I/LRIS	600
	8481	143	P60/SEDM	1200		9583	448	P60/SEDM	2160
	8481	144	LT/SPRAT	1000		9586	451	P60/SEDM	2160
	8534	195	P60/SEDM	1200	SN 2020xtg	9226	91	P60/SEDM	2160
SN 2019agi	8547	42	UH88/SNIFS	1820		9491	340	Keck I/LRIS	600
SN 2019ibk	8691	35	P60/SEDM	2250		9606	448	Keck I/LRIS	1200
	8695	39	P60/SEDM	2250	SN 2020abfe	9189	27	P60/SEDM	2700
	8697	41	P60/SEDM	2250		9319	146	Keck I/LRIS	400
	8748	90	P60/SEDM	2250	SN 2020aekp	9224	19	P60/SEDM	2160
	8761	103	P200/DBSP	600		9342	132	P60/SEDM	2160
SN 2019rvb	8766	14	P60/SEDM	2250		9343	132	NOT/ALFOSC	1200
	8780	26	P200/DBSP	600		9362	151	P60/SEDM	2700
SN 2020onv	9058	23	P60/SEDM	1800		9381	169	NOT/ALFOSC	2400
	9062	27	P60/SEDM	1800		9404	191	P60/SEDM	2700
	9069	33	P60/SEDM	1800		9425	211	NOT/ALFOSC	1800
	9070	34	LT/SPRAT	750		9434	220	P60/SEDM	2700
	9073	37	P60/SEDM	1800		9448	233	P60/SEDM	2700
	9074	38	NOT/ALFOSC	450		9468	252	P60/SEDM	2700
SN 2020qzx	9076	13	P60/SEDM	2250		9569	348	P60/SEDM	2700
	9087	22	P60/SEDM	2250					
	9092	26	NOT/ALFOSC	1800					
	9098	32	P60/SEDM	2250					
	9101	34	NOT/ALFOSC	1200					
	9107	40	P200/DBSP	900					
	9112	45	Keck I/LRIS	300					
	9121	53	P60/SEDM	2250					
	9141	71	Keck I/LRIS	399					

Table 4

Explosion Time Epoch Estimates Derived from Prepeak Multiband Light Curves

IAU Name	PL Fit Filters	t_o (MJD)	1σ Interval (days)
SN 2018crl	g, r, o	58,271.83	[−0.48,+0.38]
SN 2018gkx	r, o	58,371.34	[−0.64,+0.53]
SN 2018evt	...	58,334.26	[−2.00,+2.00]
SN 2019agi	...	58,502.48	[−1.51,+1.51]
SN 2019ibk	...	58,654.61	[−2.99,+2.99]
SN 2019rvb	g, r, i, o	58,749.16	[−0.79,+0.60]
SN 2020onv	o	59,032.75	[−2.49,+1.10]
SN 2020qzx	g, r, o	59,063.05	[−0.51,+0.45]
SN 2020uem	...	59,117.03	[−56.63,+56.63]
SN 2020xtg	...	59,130.14	[−0.04,+0.04]
SN 2020abfe	g, r, o	59,159.36	[−2.16,+2.23]
SN 2020aekp	...	59,204.53	[−5.50,+5.50]

Note. For six out of the 12 SNe Ia-CSM, we were able to fit a PL model to the multiband data following Miller et al. (2020). For the remaining six SNe, the explosion epoch was estimated by taking the mean of the first 5σ detection and last upper limit before the first detection.

mid-IR luminosity can be fainter than these limits for SNe Ia-CSM (as can be seen for other nearby SNe in this sample) and SN 2020abfe is at a redshift of 0.093, it might just be out of reach for WISE.

The brightness of SNe Ia-CSM in the mid-IR can be indicative of existing or newly formed dust. A clear signature of new dust is reduced flux in the red wing of the $H\alpha$ emission line at late phases as the new dust formed in the cold dense shell (CDS) behind the forward shock absorbs the far-side (redshifted) intermediate and narrow-line emission (see the bottom panel of Figure 7). For our sample, this reduction in the $H\alpha$ red wing is the most pronounced for SN 2018evt.

3.1.5. Bolometric Luminosity

As SNe Ia-CSM luminosity is dominated by CSM interaction, their spectra comprise a pseudo-continuum on the blue side and strong $H\alpha$ emission on the red side; hence a blackbody fit to multiband photometric data is not appropriate to estimate their bolometric luminosities. Instead we calculate a pseudo-bolometric luminosity from the available multiband optical data by linearly interpolating the flux between the bands and

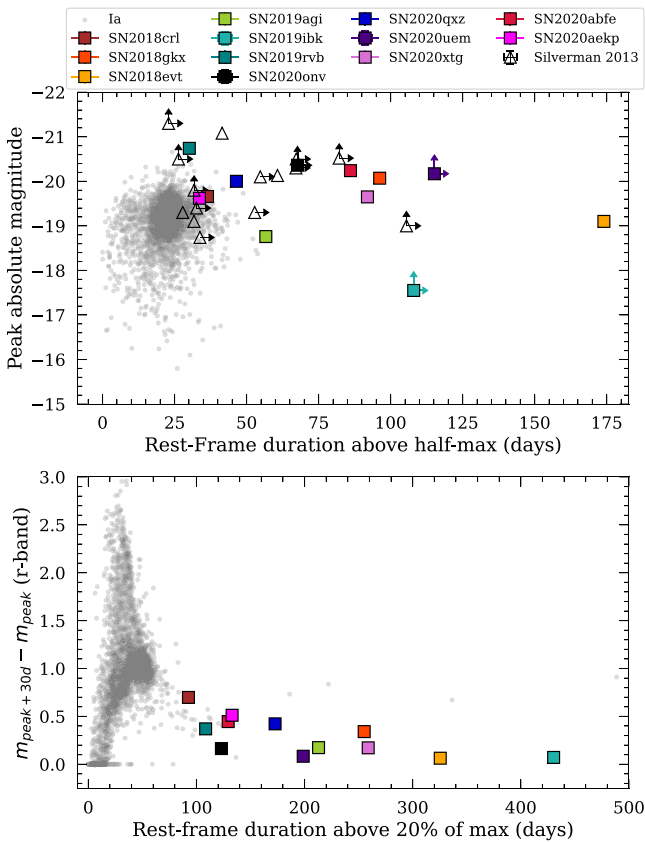


Figure 2. Top: location of our 12 SNe Ia-CSM in the peak absolute magnitude vs. rest-frame duration above half-max phase space. The colored points are the BTS SNe Ia-CSM and the gray points are the rest of the BTS SNe Ia. Also shown with empty triangles are the SNe Ia-CSM from S13. The vertical arrows mark the upper limits to the peak absolute magnitudes and the horizontal arrows mark the lower limits to the durations of SNe not having prepeak coverage. Bottom: change in magnitude 30 days after peak (Δm_{30}) vs. rest-frame duration above 20% of the peak flux for BTS SNe Ia and SNe Ia-CSM. These criteria were used to filter out potential SNe Ia-CSM from all SNe Ia and demonstrate that SNe Ia-CSM occupy a distinct portion in this phase space. However some gray points (not SN Ia-CSM) remain on the longer-duration side and are the false-positive cases described in Section 2.1.

integrating over the optical wavelength range spanned by the ATLAS and ZTF bands. The individual band light curves are first interpolated using Gaussian process regression to fill in the missing epochs. This estimate places a strict lower limit on the bolometric luminosity.

In Figure 5 we show the pseudo-bolometric luminosity of our SN Ia-CSM sample in comparison with SN 1991T (Type Ia) and SNe 1997cy, 1999E, 2002ic, 2005gj, 2013dn, and PTF11kx (Ia-CSM). Multiband photometric data were taken from the Open Supernova Catalog (Guillochon et al. 2017) for SN 1991T (Filippenko et al. 1992; Ford et al. 1993; Schmidt et al. 1994) to generate the bolometric luminosity light curve through blackbody fitting. The pseudo-bolometric luminosity light curve for SN 1997cy was obtained from Germany et al. (2000), for SN 2013dn from Fox et al. (2015), and for SNe 2002ic, 2005gj, 1999E, and PTF11kx from Inserra et al. (2016).

All BTS SNe Ia-CSM show a slow evolution in bolometric luminosity, inconsistent with the decay of ^{56}Co to ^{56}Fe . The sample’s overall luminosity decline rates are comparable to those of SNe 1997cy and 2013dn, as shown in Figure 5. Only SNe 2018crl and 2020aekp seem to show early decline in their

pseudo-bolometric light curves similar to SN 1991T for about 40 days after peak, like SN 2002ic and PTF11kx. Another BTS interacting SN Ia, ZTF20aatxryt (Kool et al. 2022), was found to follow the PTF11kx light-curve evolution very closely and as its light curve fell into a plateau the SN started showing signs of interaction with a helium-rich CSM and evolved into a helium-rich SN Ia-CSM. We have excluded ZTF20aatxryt from the sample as we focus on typical SNe Ia-CSM interacting with a hydrogen-rich CSM in this study. At late phases (~ 300 days), the SNe Ia-CSM are approximately 100 times brighter than normal SNe Ia at the same epoch. Therefore, at these late phases, the luminosity and spectral features of SNe Ia-CSM are entirely dominated by CSM interaction with little emergent SN flux. From the pseudo-bolometric light curves, we place a lower limit on the total radiated energy for SNe Ia-CSM of $0.1\text{--}1.5 \times 10^{50}$ erg. This is well below the thermonuclear budget ($E_{\text{kin}} \sim 10^{51}$ erg), but as this is a lower limit and some SNe in the sample have unconstrained peaks, the true total radiative energy might come close to the thermonuclear budget, requiring high conversion efficiencies to achieve their luminosity.

3.2. Spectroscopy

Figure 6 displays the spectral series obtained for the BTS SNe Ia-CSM. Most of the early-time spectra were taken with SEDM, the BTS workhorse instrument ($R \sim 100$), which is not able to resolve narrow CSM lines. Therefore, these SNe were followed up with higher-resolution instruments to get more secure classifications. For each spectrum in Figure 6, the phase is provided with respect to the explosion epoch estimate given in Table 4. We have spectra ranging from a few to around 470 days from explosion. Considering the well-constrained explosion time of SN 2018evt, presence of narrow $\text{H}\alpha$ in its first spectrum at 8 days since explosion and assuming a typical ejecta velocity of $\sim 20,000 \text{ km s}^{-1}$, this implies that the CSM interaction started as close as $\sim 1.4 \times 10^{15}$ cm.

Figure 7 shows the early-time (left) and late-time (right) spectral behavior of the BTS SNe Ia-CSM together with a few historical SNe for comparison, namely SNe Ia-CSM SN 2011jb (S13), SN 2005gj, and PTF11kx, the Type Ia SN 1991T and the well-observed Type II_n SN 2010jl. Vertical gray regions mark typical SN Ia absorption features and [Fe II/III]-line regions, and vertical dashed lines mark Balmer emission lines. The sample spectra have been multiplied by a constant factor to magnify relevant spectral features. In the following paragraphs, we compare the observations of some of the spectral features with previous analyses of this class (S13; Fox et al. 2015; Inserra et al. 2016).

A few of our early-time SNe Ia-CSM show underlying SN Ia absorption features like SNe PTF11kx and 2002ic (most are, however, quite diluted and also affected by the low resolution and signal-to-noise ratio (S/N) of the SEDM spectra), the most notable being SNe 2018evt, 2020qvx, and 2020aekp. SNe 2020qvx and 2020aekp also have among the fastest initial postpeak decline rates in the sample, similar to PTF11kx, while coverage around peak is not available for SN 2018evt. On the other hand, SNe with slower decline rates similar to SN 1997cy and SN 2005gj have more SN II_n-like early-time spectra dominated by a blue pseudo-continuum and Balmer emission. The faster decline rates suggest we are still seeing some of the emission from the ejecta at those phases. To unveil the nature of the progenitors of interacting SNe, it is therefore necessary

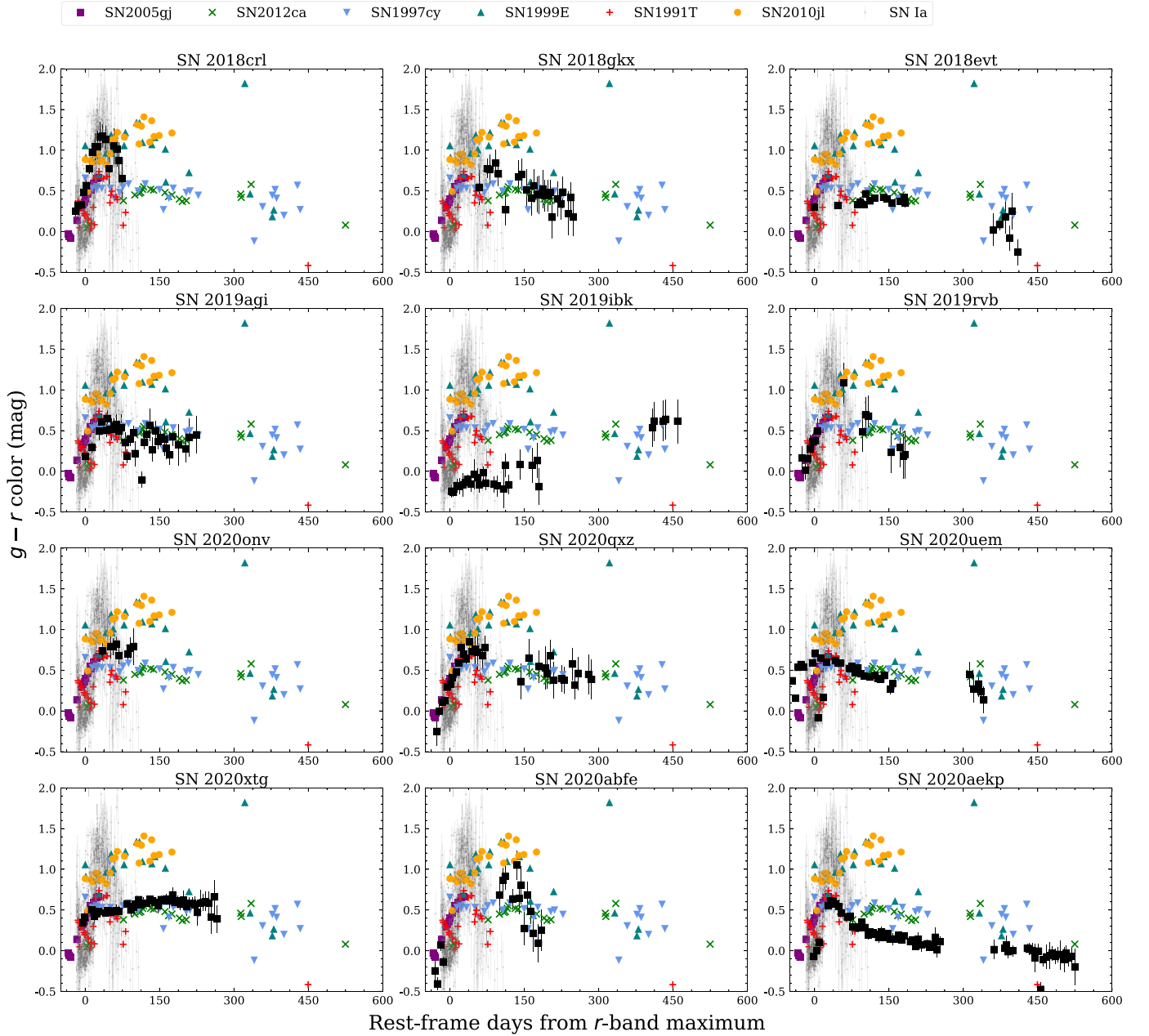


Figure 3. Color evolution ($g - r$) of the BTS SNe Ia-CSM from r -band maximum (plotted in black) compared with SNe 2005gj, 1997cy, 1999E (Ia-CSM), SN 2012ca (IIn/Ia-CSM), SN 2010jl (IIn), SN 1991T (SN Ia), and ZTF SNe Ia (gray lines). As can be seen for up to ~ 150 days, our SNe Ia-CSM tend to be redder than SNe Ia and at late times develop a plateau similar to other interacting SNe (IIn/Ia-CSM).

to obtain some spectroscopic follow up before peak light. Spectroscopic data at the phase of transition to interaction-dominated luminosity would also help in deducing the extent and density structure of the optically thick CSM.

Late-time spectra of SNe Ia-CSM look very similar to those of SNe IIn, heavily dominated by $H\alpha$ emission. The CSM interaction masks the underlying SN signature and we instead see late-time spectra riddled with photoionized CSM lines. In some cases, the photosphere might lie in an optically thick CDS formed between the forward and reverse shocks which obscures the ejecta completely (Chugai et al. 2004; Smith et al. 2008). The continuum is also enshrouded under a blue quasi-continuum from a forest of iron-group element lines (S13) as identified and analysed for SNe 2012ca and 2013dn by Fox et al. (2015).

The blue quasi-continuum blend of iron lines ([Fe III] lines around ~ 4700 Å and [Fe II] around ~ 5200 Å) in the spectra of the BTS SN Ia-CSM sample (see Figure 7, top right panel) is the dominant feature blue-ward of 5500 Å but the ratio of [Fe III]/[Fe II] is much weaker compared to that of SNe Ia (like SN 1991T). This feature is more apparent in the SNe Ia-CSM like PTF11kx and SN 2002ic that became interaction-dominated later than for other SNe Ia-CSM such as SNe 1997cy, 1999E, and 2012ca (SN Ia-CSM/IIn, for which a clear type has not been established). Inserra et al. (2014) argues for a CC origin for SN 2012ca given the low amount of [Fe III] along with the detection of blueshifted carbon and oxygen lines (which however, were later argued to be [Fe II] lines by Fox et al. 2015). S13 instead argues in favor of a thermonuclear origin given the presence of this blue quasi-continuum, despite

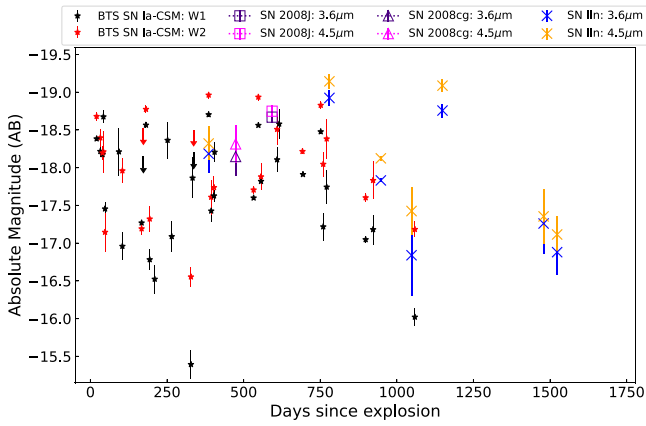


Figure 4. unWISE detections in the W1 and W2 bands of the BTS SNe Ia-CSM. The W1 and W2 points are marked with black and red filled stars, respectively. Spitzer IRAC photometry of SNe IIn (blue and orange crosses) and two SNe Ia-CSM from Fox et al. (2011) (SNe 2008cg and 2008J, shown with empty triangles and squares, respectively) are also shown for comparison. Nine out of the 12 BTS SNe Ia-CSM are as bright in the mid-IR as other interacting SNe (~ -16 to ~ -19). The upper limits for SN 2020abfe are shown in black and red filled upside-down triangles.

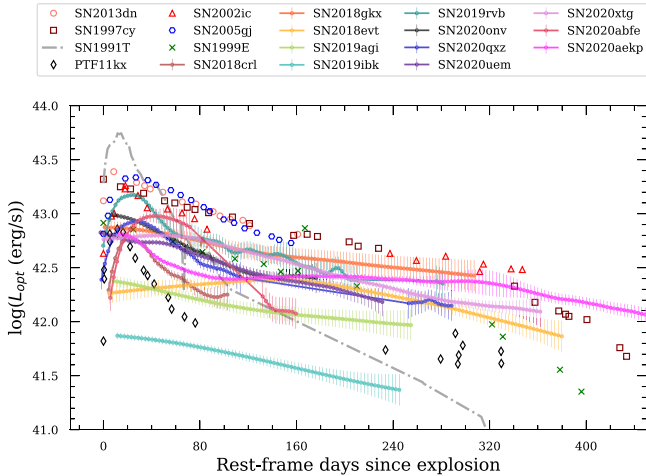


Figure 5. Pseudo-bolometric luminosity light curves of the BTS SNe Ia-CSM compared with the pseudo-bolometric light curves of SNe 1991T, 1997cy, 1999E, 2002ic, 2005gj, 2013dn, and PTF11kx from the literature. The light curves in each filter having more than 10 epochs were interpolated using Gaussian process regression to fill in the missing epochs, and at each epoch the fluxes between the bands were linearly interpolated and integrated over the optical wavelength range spanned by the ZTF and ATLAS filters to get the pseudo-bolometric luminosity. For the BTS SNe, the phases are with respect to the estimated explosion epochs, while for the comparison SNe the phases are with respect to discovery.

[Fe III] being weaker. Fox et al. (2015) points out that a similarly suppressed ratio of [Fe III]/[Fe II] is observed in some SNe Ia, particularly the superChandra candidate SN 2009dc, for which the explanation was suggested to be a low ionization nebular phase owing to high central ejecta density and low expansion velocities (Taubenberger et al. 2013). Fox et al. (2015) argue that in the case of SNe Ia-CSM, a lower ionization state could arise owing to the deceleration of ejecta by the dense CSM, explaining the Fe line ratio suppression. Since Ca has lower first and second ionization potentials than Fe, the detection of [Ca II] $\lambda\lambda 7291, 7324$ would be consistent with this low ionization, which Fox et al. (2015) confirms for SNe 2012ca and 2013dn. Indeed, we find clear evidence of [Ca II] emission for eight out of the 12 SNe in our sample and

moderate to weak signals for the remaining four. Although this does favor the argument for a thermonuclear origin, a similar blue quasi-continuum is also observed in other interacting SN types like SNe IIn (SN 2006jc, Foley et al. 2007) and SNe IIn (SNe 2005ip and 2009ip), making Fe an incomplete indicator of the progenitor nature (see the detailed discussion in Fox et al. 2015).

We do not find strong evidence of O I $\lambda 7774$ or [O I] $\lambda\lambda 6300, 6364$ emission in our sample, although they might be present at very weak levels in some SNe (e.g., SN 2020uem). SN 2020uem has strong emission lines at 6248, 7155, and 7720 Å, which are consistent with being iron lines and were also observed in SNe 2012ca, 2013dn, and 2008J. S13 note that the very broad emission around 7400 Å can be due to a blend of [Ca II] $\lambda\lambda 7291, 7324$ and [O II] $\lambda\lambda 7319, 7330$, however we note that this broad emission is likely to be from calcium as O II is harder to excite than O I, which is either very weak or absent in our spectra. The broad Ca NIR triplet feature resulting from electron scattering is the next strongest feature after the Balmer emission and is present in all mid- to late-time spectra of the SNe in our sample where the wavelength coverage is available. We observe it increasing in relative strength with phase, at least for a year, after which we no longer have spectral coverage.

The bottom panel of Figure 7 shows the line profile of $H\alpha$, with the blue side reflected over the red side at the maximum flux after continuum removal. We do see evidence of diminished flux in the red wing of $H\alpha$ at late phases in some SNe (most notable in SNe 2018evt and 2020uem), which can indicate the formation of new dust in the postshocked CSM. S13 claim to observe this for all non-PTF SNe Ia-CSM in their sample starting at ~ 75 – 100 days, while for the PTF SNe Ia-CSM they do not have spectra available post that phase range. For some BTS SNe Ia-CSM, we also do not have spectra available post 100 days, which limits any analysis of this phenomenon for a large enough sample.

The spectra were reduced and processed as outlined in Section 2.5 for the emission-line analysis, the results of which are described in the next section. We used only good S/N SEDM spectra and intermediate-resolution spectra for line identification and analysis.

3.2.1. $H\alpha$, $H\beta$, and He I Emission Lines

To analyse the $H\alpha$ line emission, we first fit the continuum level using the `fit_continuum` function of the `specutils` Python package, where the continuum is estimated by a cubic function fitted to regions on each side of the line. We remove this continuum level and then fit the $H\alpha$ line with a broad and a narrow-component Gaussian function using the `fit_lines` function of `specutils`, which returns the best-fit Gaussian model and the 1σ uncertainties of the model parameters. We generate 1000 sample models within the 1σ uncertainties of the parameters centered around the best-fit values and calculate the intensity, flux, and velocity (FWHM) of the broad and narrow components for each model. Then we take the median and standard deviation of the intensity, flux, and velocity FWHM distributions to get their final best values and 1σ uncertainties. The equivalent width (EW) was also calculated for the $H\alpha$ line using the model fit as well as directly from the data, and the difference between the values derived from the model and data is reported as the error on the EW. All values are reported in Table 5. For three SNe in our sample, we have a series of intermediate-resolution spectra through which

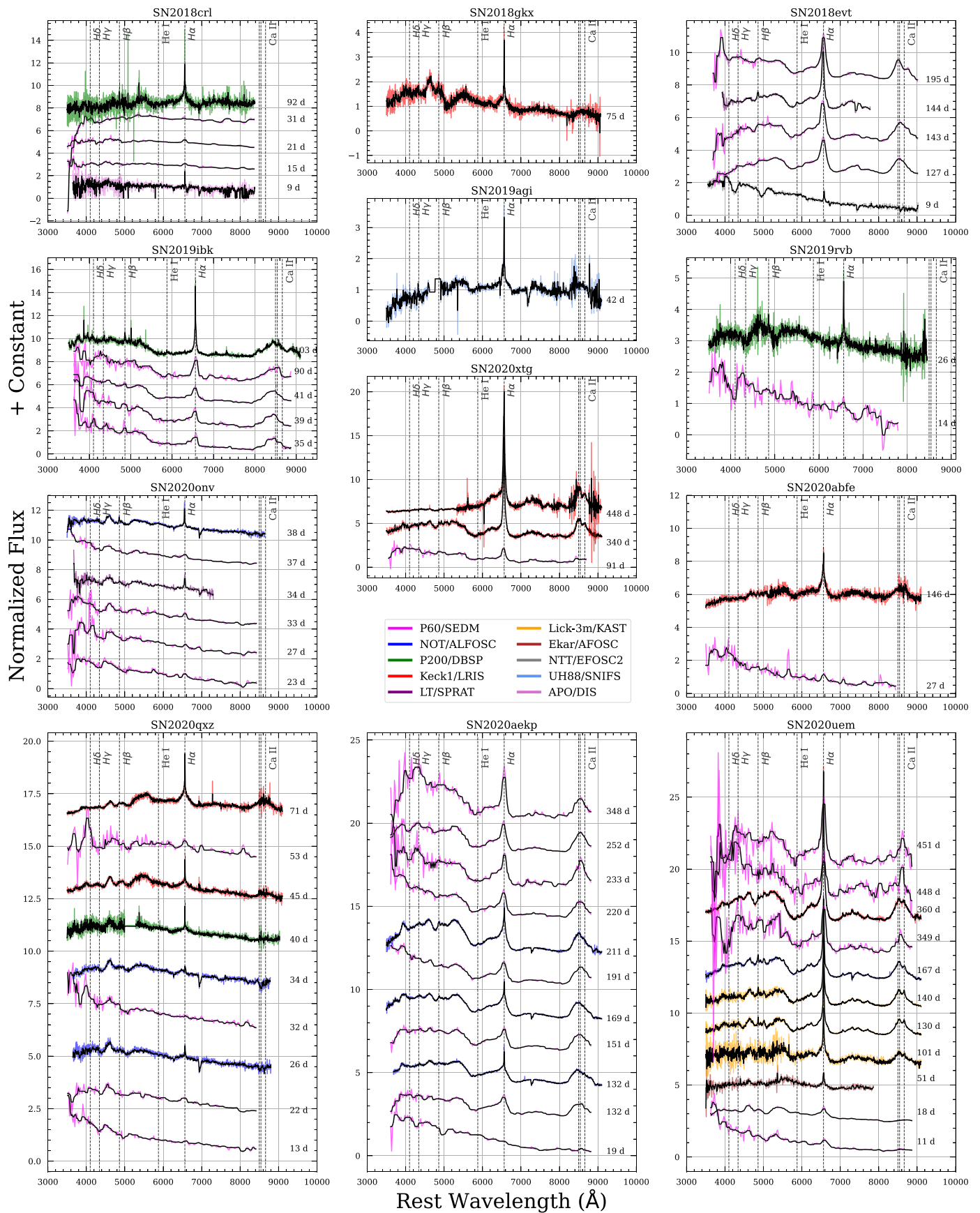


Figure 6. Spectral series of all SNe Ia-CSM presented in this paper. The rest-frame phases are shown alongside the spectra in each subplot and have been calculated using the explosion epoch estimates. The colors depict different instruments used to obtain these data. Major emission lines are marked with vertical dashed lines.

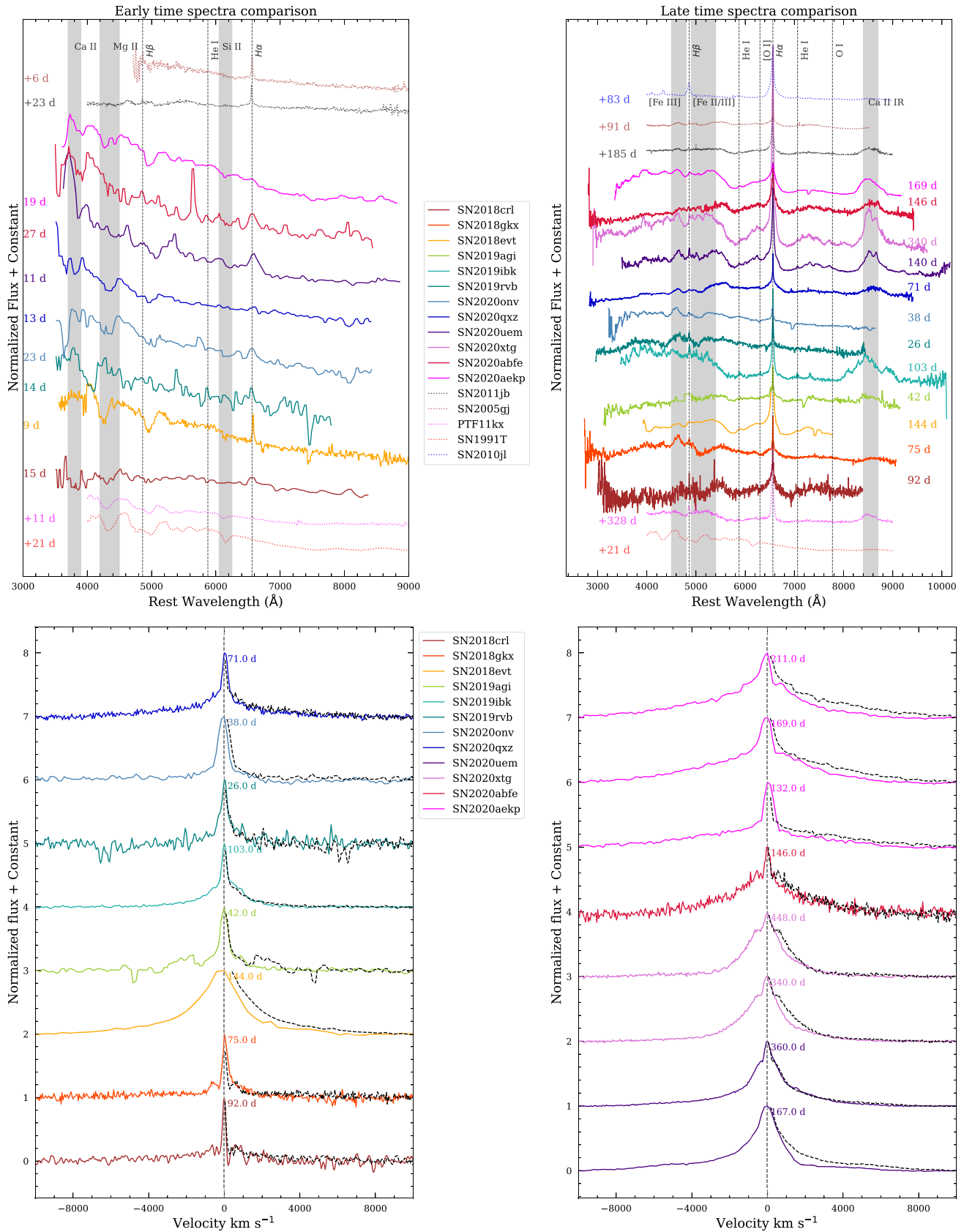


Figure 7. Top left: early-time spectra of BTS SNe Ia-CSM with phases between 0 and 30 days since explosion compared to the spectra of SNe 2011jb, 2005gj, 1991T, and PTF11kx (phases in days since discovery). Top right: late-time spectra of BTS SNe Ia-CSM (phases ranging from 40 to 370 days since explosion) compared to the spectra of SNe 2011jb, 2005gj, 2010jl, and PTF11kx (phases in days since discovery). Bottom left and right: H α line profiles (post continuum removal) with the blue side reflected across the peak flux, marked by dashed lines. SNe 2020aekp, 2020abfe, 2020xtg, and 2020uem are shown in the right panel, and SNe 2018crl, 2018gkx, 2018evt, 2019agi, 2019ink, 2019rbv, 2020onv, and 2020qxz are displayed in the left panel.

Table 5
Summary of the H α Line Properties Obtained from the Two-component Gaussian Fitting

SN Name	Phase (days)	Broad Flux (10^{-16} erg s $^{-1}$ cm $^{-2}$)	Narrow Flux (10^{-16} erg s $^{-1}$ cm $^{-2}$)	Total Flux (10^{-16} erg s $^{-1}$ cm $^{-2}$)	Broad Velocity FWHM (km s $^{-1}$)	Narrow Velocity FWHM (km s $^{-1}$)
SN 2018crl	92	135.4 \pm 10.0	32.8 \pm 2.0	168.2 \pm 12.0	4137 \pm 312	<214
SN 2018gkx	75	9.9 \pm 0.7	3.9 \pm 0.2	13.7 \pm 0.9	2640 \pm 398	<375
SN 2018evt	144	2020.3 \pm 128.5	1247.4 \pm 52.8	3267.7 \pm 181.3	6465 \pm 997	1816 \pm 973
SN 2019agi	42	52.7 \pm 3.6	23.7 \pm 1.1	76.4 \pm 4.7	3836 \pm 349	464 \pm 301
SN 2019ibk	103	85.6 \pm 1.7	17.0 \pm 0.5	102.6 \pm 2.3	2431 \pm 217	272 \pm 214
SN 2019rvb	26	22.0 \pm 3.0	10.4 \pm 1.0	32.5 \pm 4.1	2321 \pm 298	374 \pm 216
SN 2020onv	38	32.8 \pm 5.2	33.3 \pm 2.0	66.1 \pm 7.2	2714 \pm 879	<834
SN 2020qzx	26	76.6 \pm 6.2	13.8 \pm 1.7	90.4 \pm 7.9	11294 \pm 1106	<836
SN 2020qzx	34	55.1 \pm 5.0	10.8 \pm 1.8	65.9 \pm 6.8	8252 \pm 1039	1070 \pm 845
SN 2020qzx	40	12.9 \pm 1.7	7.6 \pm 0.5	20.5 \pm 2.2	2049 \pm 284	245 \pm 215
SN 2020qzx	45	20.7 \pm 1.6	9.1 \pm 0.4	29.8 \pm 2.1	3429 \pm 419	<375
SN 2020qzx	71	39.1 \pm 1.3	10.4 \pm 0.4	49.5 \pm 1.7	5013 \pm 395	400 \pm 375
SN 2020uem	51	246.3 \pm 47.2	151.1 \pm 16.8	397.4 \pm 64.0	6520 \pm 1163	1178 \pm 840
SN 2020uem	101	655.2 \pm 28.9	241.2 \pm 9.6	896.4 \pm 38.4	7456 \pm 309	1066 \pm 217
SN 2020uem	130	552.9 \pm 17.6	281.8 \pm 6.2	834.8 \pm 23.8	7465 \pm 265	1269 \pm 215
SN 2020uem	140	545.4 \pm 20.0	283.4 \pm 6.8	828.8 \pm 26.7	7457 \pm 275	1308 \pm 216
SN 2020uem	167	424.3 \pm 19.0	312.0 \pm 7.7	736.3 \pm 26.6	6852 \pm 854	1439 \pm 834
SN 2020uem	360	179.8 \pm 4.0	77.4 \pm 1.4	257.2 \pm 5.4	5377 \pm 382	1170 \pm 375
SN 2020xtg	340	129.2 \pm 4.2	52.1 \pm 1.6	181.3 \pm 5.8	4242 \pm 382	1258 \pm 376
SN 2020xtg	448	131.7 \pm 7.7	96.3 \pm 3.2	228.0 \pm 10.9	4452 \pm 395	1566 \pm 377
SN 2020abfe	146	33.6 \pm 1.1	3.0 \pm 0.3	36.6 \pm 1.4	4411 \pm 389	<376
SN 2020aekp	132	149.5 \pm 4.0	33.0 \pm 1.0	182.5 \pm 5.0	7728 \pm 846	<833
SN 2020aekp	169	231.0 \pm 4.5	32.3 \pm 1.3	263.3 \pm 5.8	6775 \pm 839	<834
SN 2020aekp	211	251.0 \pm 9.5	58.6 \pm 3.4	309.6 \pm 12.8	7422 \pm 852	1342 \pm 836

we can trace the evolution of the H α line with phase. Figure 8 shows this trend of the H α line parameters (integrated flux in the top panel and EW in the bottom panel) versus phase for all SNe in our sample. The unfilled markers represent the narrow emission while the filled markers represent the broad emission. For SNe where this analysis could be done on multiple spectra, we see that the H α EW generally increases over time, with some SNe showing fluctuations up to 100 days, possibly due to the interaction of ejecta with multiple CSM shells of varying density. For SN 2018evt, Yang et al. (2022) analysed H α line properties from a comprehensive spectral series data set, which are plotted in Figure 8 in gray circles and seem to agree well with our analysis at comparable epochs.

From the Gaussian profile line fitting analysis of the H α emission line, we found that the broader component has velocities ranging from ~ 1000 to ~ 4000 km s $^{-1}$ (intermediate width) and the narrow component has velocities of about ~ 200 to ~ 1000 km s $^{-1}$ (see Figure 9). The narrow component could only be resolved down to ~ 300 km s $^{-1}$ limited by the mediocre resolution of the spectrographs used (Keck I/LRIS $R \sim 800$; P200/DBSP $R \sim 1000$; NOT/ALFOSC has $R \sim 360$). While we know that the narrow lines originate in the unshackled ionized CSM, the exact origin of the intermediate components is uncertain. They could arise from the postshock gas behind the forward shock or from the shocked dense clumps in the CSM (Chugai & Danziger 1994).

The luminosities of the H α line measured from the BTS SNe Ia-CSM lie in the range $2.5\text{--}37 \times 10^{40}$ erg s $^{-1}$, which are comparable to the values from S13 who reported most of their SNe in the $1\text{--}10 \times 10^{40}$ erg s $^{-1}$ range except one object that had a luminosity of 39×10^{40} erg s $^{-1}$. With the broad H α luminosities, we did a simple estimate of the mass-loss rate assuming a spherically symmetric CSM deposited by a stationary wind with $\rho \propto r^{-2}$ and velocity v_w (Chugai 1991;

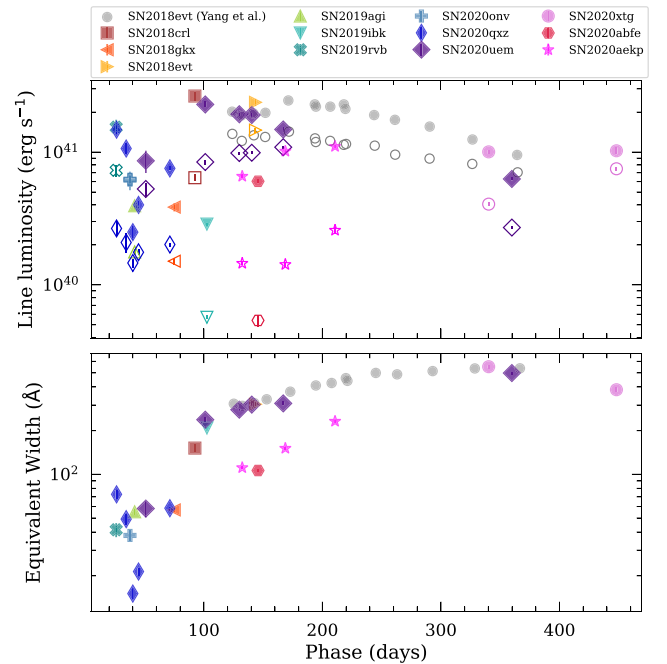


Figure 8. Integrated fluxes and EWs of the H α emission line with respect to the SN phase for the BTS SN Ia-CSM sample. Broad-component values are shown with filled markers and narrow-component values with unfilled markers. SN 2018evt's H α luminosities and EWs, presented in Yang et al. (2022), are also shown in gray circles.

Salamanca et al. 1998). The mass-loss rate \dot{M} can be related to the broad H α luminosity $L_{\text{H}\alpha}^{\text{Broad}}$ as (Equation (2) of Salamanca et al. 1998)

$$L_{\text{H}\alpha}^{\text{Broad}} = \frac{1}{4} \epsilon_{\text{H}\alpha} \frac{\dot{M}}{v_w} v_s^3,$$

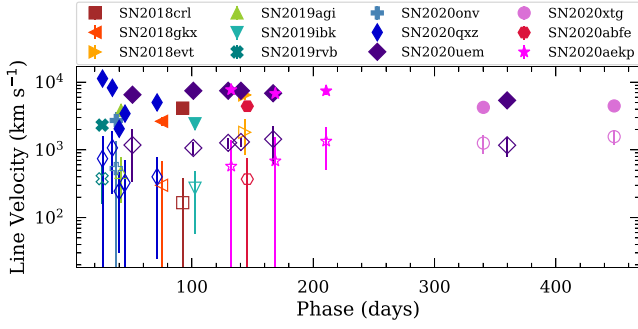


Figure 9. Velocity of the $H\alpha$ emission line with respect to the SN phase for the BTS SN Ia-CSM sample. Broad-component values are shown with filled markers and narrow-component values with unfilled markers.

where v_s is the shock velocity (obtained from the broad-component velocity of the $H\alpha$ line). We used a value of 100 km s^{-1} considering previous high-resolution spectral studies of SNe Ia-CSM (Kotak & Meikle 2005; Aldering et al. 2006; Dilday et al. 2012) for v_w as we cannot fully resolve the narrow component and a maximum value of 0.1 for the efficiency factor $\epsilon_{H\alpha}$ (Salamanca et al. 1998). The mass-loss rates were estimated from the available spectra and are shown in Figure 10 as a function of years before explosion ($t_w = \frac{v_s t}{v_w}$, where t is the phase of the spectrum). For most SNe in the sample, the mass-loss rates lie between 0.001 and $0.02 M_\odot \text{ yr}^{-1}$, except for SN 2019rbv, which has $\sim 0.07 M_\odot \text{ yr}^{-1}$ lost within 2 yr prior to explosion. These rates are much higher than what could be attained from a red giant superwind ($\sim 3 \times 10^{-4} M_\odot \text{ yr}^{-1}$) but are comparable to previous estimates (calculated through multiple methods) for SNe Ia-CSM and require some unusual mechanism to reach such persistently higher mass-loss rates in the decades prior to explosion. Also to consider is that the simplistic assumption of spherical symmetry likely does not apply for SNe Ia-CSM. Evidence of multiple thin shells and an asymmetric CSM was observed for PTF11kx (Dilday et al. 2012), and light-curve modeling of SNe 1997cy and 2002ic suggested a better fit to a flat density profile rather than stationary wind (Chugai & Yungelson 2004). An asymmetric or clumpy CSM might be the norm for SNe Ia-CSM (and some SNe IIn) rather than the exception.

The same analysis as for the $H\alpha$ line was also carried out for $H\beta$ and He I $\lambda 5876$ with a one-component Gaussian fit. For cases where a Gaussian model could not fit the data, we integrate the flux value in a 100 \AA region centered at 5876 \AA for He I. Na I D absorption lines are also prevalent in some spectra and blend with the He I line, resulting in positive EWs for some SNe. The cumulative distributions of $H\beta$ and He I EWs are shown in the top and bottom panels of Figure 11, respectively.

The $H\beta$ median EW measured from the BTS SN Ia-CSM sample is 7.1 \AA , close to the S13 value of $\sim 6 \text{ \AA}$ and quite weak compared to what S13 measured for SNe IIn ($\sim 13 \text{ \AA}$). The overall cumulative distribution of the $H\beta$ EWs is also comparable to those of the S13 SNe Ia-CSM rather than to the S13 SNe IIn. For the He I $\lambda 5876$ line, the median EW measured for our BTS SN Ia-CSM sample, considering only significant emission features, is 2.4 \AA . This is close to the value of $\sim 2 \text{ \AA}$ reported in S13, and again significantly different from their SN IIn value of $\sim 6 \text{ \AA}$ ($\sim 4 \text{ \AA}$ with upper limits), however

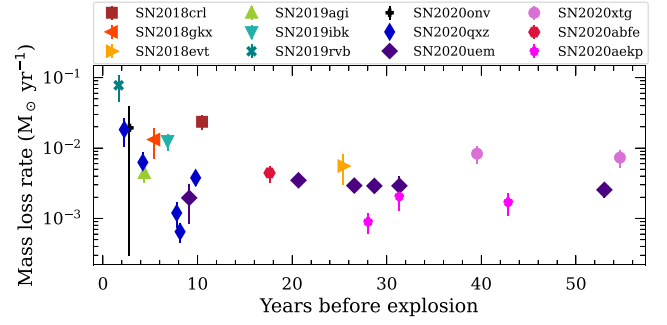


Figure 10. Mass-loss rates estimated from the luminosity of the broad component of $H\alpha$ for the BTS SNe Ia-CSM. A value of 100 km s^{-1} was assumed for the wind velocity.

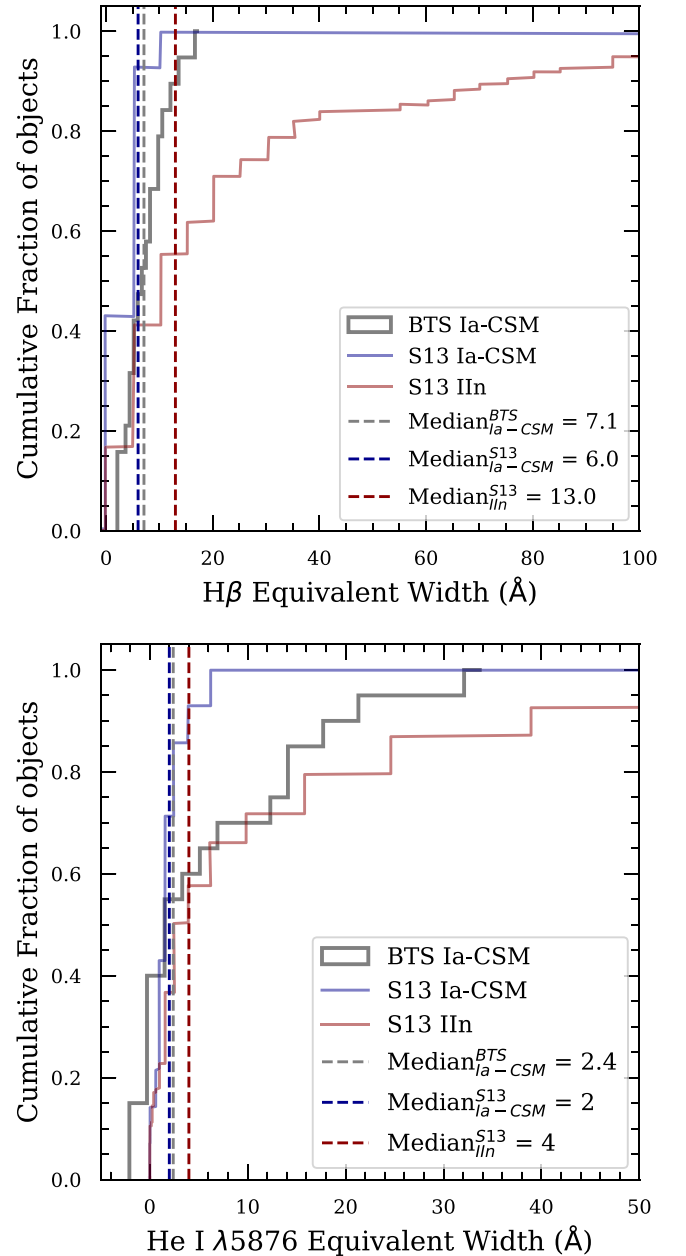


Figure 11. Cumulative distributions of the EWs of the $H\beta$ and He I $\lambda 5876$ emission lines calculated from the BTS SNe Ia-CSM (in gray) compared with the respective distributions presented in S13 for SNe Ia-CSM (blue) and SNe IIn (red). Vertical dashed lines mark the median EW of the distributions.

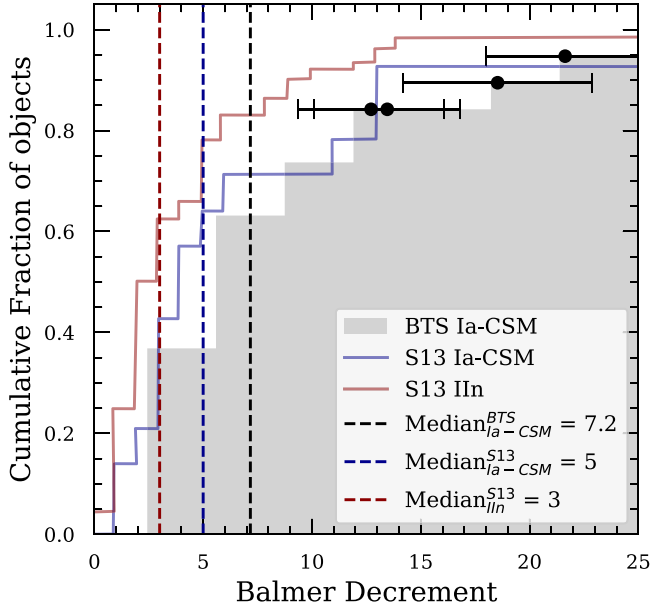


Figure 12. Cumulative distribution of $H\alpha/H\beta$ intensity ratio (Balmer decrement) calculated from intermediate-resolution spectra of the BTS SN Ia-CSM sample (gray shaded region). The red line is the distribution of the Balmer decrement of SNe IIn measured in S13 and the blue line is the SN Ia-CSM Balmer decrement distribution from S13. The black circles are a few representative points indicating the high Balmer decrement values and the uncertainties on them. The vertical dashed line is the median Balmer decrement measured from the BTS SNe Ia-CSM.

the overall distribution seems to be closer to the S13 SNe IIn (but still weaker) rather than to the S13 SNe Ia-CSM. This indicates that perhaps He I is not as good a discriminant between the populations compared to $H\beta$. Among the most He-rich SNe in our sample are SNe 2019ibk, 2020uem, 2020xtg, 2020aekp, and 2018evt, and these SNe also have the higher $H\alpha$ EWs in the sample.

Figure 12 plots the cumulative distribution of the Balmer decrements ($F_{H\alpha}/F_{H\beta}$) measured for our sample of SNe. The higher Balmer decrement values (>15) have large errors associated to them because of the low S/Ns of the spectra from which they were derived, particularly near the $H\beta$ line. Consistent with the results of S13, the SNe Ia-CSM from this sample also have a high median Balmer decrement value of ~ 7 (~ 5 in S13), indicating that the emission-line mechanism is probably collisional excitation or self absorption rather than recombination, from which the expected Balmer decrement value is ~ 3 . In the case of SNe Ia-CSM, if the CSM distribution consists of multiple shells as suggested for PTF11kx, moderately high densities could be created when fast-moving ejecta overtake slowly moving thin dense CSM shells, creating a large enough optical depth in the $H\alpha$ line which results in the $H\beta$ transition decaying as $\text{Pa}\alpha + H\alpha$ (Xu et al. 1992). For some individual SNe where multiple spectra are available, the Balmer decrement is observed to first increase and later on decrease with phase.

3.3. Host Galaxies

We retrieved science-ready coadded images from the Galaxy Evolution Explorer (GALEX) general release 6/7 (Martin et al. 2005), SDSS DR 9 (Ahn et al. 2012), Pan-STARRS1 (PS1) DR1 (Chambers et al. 2016), the Two Micron All Sky Survey

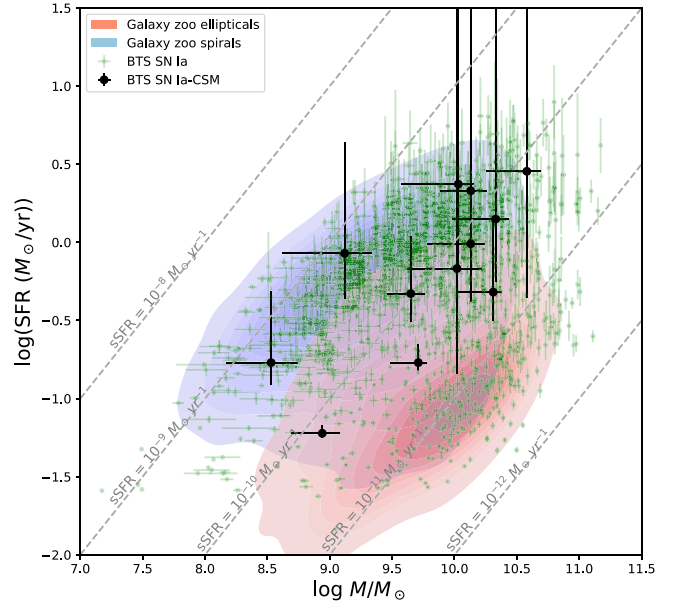


Figure 13. SFR vs. stellar mass plot of the host galaxies of the BTS SNe Ia-CSM (black circles) with Galaxy Zoo spiral (blue contours) and elliptical (red contours) galaxies for comparison. BTS SN Ia hosts are also shown for comparison in green circles. Equal specific SFR lines are marked with gray dashed lines.

(2MASS; Skrutskie et al. 2006), and preprocessed WISE images (Wright et al. 2010) from the unWISE archive (Lang 2014b).²⁷

We used the software package Lambda Adaptive Multi-Band Deblending Algorithm in R (LAMBDA; Wright et al. 2016) and tools presented in Schulze et al. (2021), to measure the brightness of the host galaxy. The spectral energy distribution (SED) was modeled with the software package Prospector²⁸ (Johnson et al. 2021). We assumed a linear-exponential star formation history, the Chabrier (2003) initial mass function, the Calzetti et al. (2000) attenuation model, and the Byler et al. (2017) model for the ionized gas contribution. The priors were set as described in Schulze et al. (2021).

Figure 13 shows the log of star formation rate (SFR) as a function of stellar mass for the hosts of the BTS SNe Ia-CSM. We also use a Galaxy Zoo (Lintott et al. 2011) sample of elliptical and spiral galaxies (randomly sampled in the redshift range $z = 0.015\text{--}0.05$), and BTS SN Ia hosts as comparison samples collected by and used for comparison in Irani et al. (2022). We find the SN Ia-CSM host galaxy population to be consistent with late-type spirals and irregulars with recent star formation histories. Four out of the 12 SNe have clearly spiral hosts, three have edge-on host galaxies, four seem to have irregulars as hosts, and one has an unclear host type. The host galaxies of 10 out of the 12 SNe have $w2 - w3$ measurements available, which are all >1 mag, putting them in the late-type category (Irani et al. 2022), one (SN 2019rvb) does not have a $W3$ measurement but has near-UV (NUV) $-PS1_r \sim 1$ mag, again putting it toward late-type, and one (SN 2020abfe) does not have any of the above information available except the PS1 r -band magnitude of 20.766, which is the faintest host galaxy (absolute SDSS r -band magnitude of -17.4) in our BTS SN Ia-CSM sample. As noted in S13, the SN Ia-CSM hosts of their

²⁷ <http://unwise.me>

²⁸ <https://github.com/bd-j/prospector> version 0.3.

sample had generally low luminosities ($-19.1 < M_r < -17.6$) except Milky Way-like spiral hosts. Our BTS SN Ia-CSM host luminosities lie in the range of $-21.8 < M_r < -17.4$, covering low to Milky Way-like luminosities.

3.4. Rates

Following the methodology used for calculating the volumetric rate of transients found in the BTS from Perley et al. (2020), we use their Equation (2) to calculate the SN Ia-CSM rate

$$R = \frac{1}{T} \sum_{i=1}^N \frac{1}{\left(\frac{4\pi}{3} D_{\max,i}^3\right) f_{\text{sky}} f_{\text{ext}} f_{\text{rec}} f_{\text{cl},i}},$$

where T is the duration of the survey, N is the number of transients that pass the quality cut, $D_{\max,i}$ is the distance out to which the i th transient with peak absolute magnitude M_i can be detected above the survey magnitude limit m_{lim} ($=19$ mag for the BTS SNe Ia-CSM) at peak light without any extinction, f_{sky} is the average active survey coverage as a fraction of full sky, f_{ext} is the average reduction in the effective survey volume due to Galactic extinction, f_{rec} is the average recovery efficiency for a detectable transient within the survey coverage area, and $f_{\text{cl},i}$ is the classification efficiency dependent on apparent magnitude.

The duration of the survey in which these 12 SNe Ia-CSM were detected is from 2018 May 1 to 2021 May 1, i.e., $T = 3$ yr. We calculate f_{sky} during this time period by averaging the sky area coverage of the public MSIP survey considering a 3 day cadence for ZTF Phase I (2018 May 1 to 2020 October 31) and 2 day cadence for ZTF Phase II (since 2020 May 1), which turns out to be $12,505 \text{ deg}^2$ for Phase I and $14,831 \text{ deg}^2$ for Phase II, giving a mean $f_{\text{sky}} = 0.32$. We use the same value of 0.82 for f_{ext} as calculated in Perley et al. (2020) given there has not been any change in the number and positions of the ZTF fields.

To estimate f_{rec} , we consider SNe Ia-CSM brighter than -18.5 peak absolute magnitude and brighter than 18 apparent magnitude (total of five), of which four pass the quality cut, giving an f_{rec} of 0.8. We take a classification completeness of 0.75 at 19 mag, 0.9 at 18.5 mag, and 1 at 17.2 mag and linearly interpolate in between these values to get $f_{\text{cl},i}$.

Then using $H_0 = 70 \text{ km s}^{-1} \text{ Mpc}^{-1}$, ignoring cosmological effects²⁹ as in Perley et al. (2020) and applying a uniform K-correction ($K = 2.5 \times \log_{10}(1+z)$), we get a rate of $29.35_{-21.37}^{+27.53} \text{ Gpc}^{-3} \text{ yr}^{-1}$ for SNe Ia-CSM. We also calculate a SN Ia rate of $2.88_{-0.25}^{+0.28} \times 10^4 \text{ Gpc}^{-3} \text{ yr}^{-1}$ for the SNe Ia observed in the same period following the same method, which is close to the value of $2.35 \times 10^4 \text{ Gpc}^{-3} \text{ yr}^{-1}$ calculated in Perley et al. (2020). This puts SNe Ia-CSM at 0.02%–0.2% of all SNe Ia. However this rate estimate should be considered a lower limit given various caveats in the correct identification of SNe Ia-CSM (see the discussion Section 4.3). If the ambiguous classification cases outlined in the Appendix are considered to be SNe Ia-CSM and included in the rate calculation, we obtain a rate upper limit of $97.7_{-77.3}^{+135.8} \text{ Gpc}^{-3} \text{ yr}^{-1}$, which is 0.07%–0.8% of all SNe Ia.

²⁹ Contraction of the control time window approximately compensated by an increase in the SFR density in the low-redshift regime for redshift-dependent SN rates.

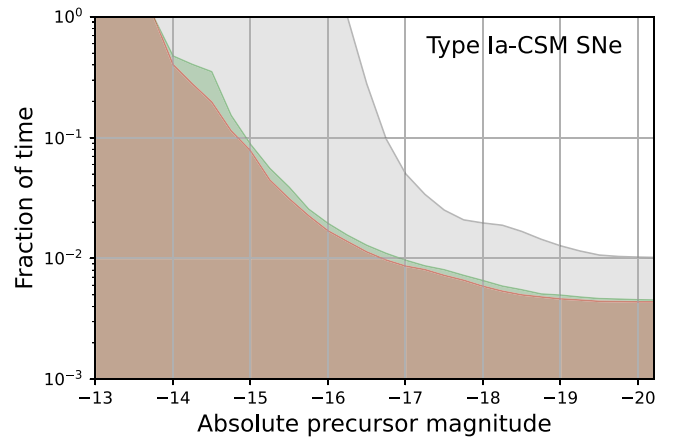


Figure 14. Precursor rate as a function of magnitude calculated from the BTS SN Ia-CSM preexplosion ZTF forced photometry stacked in 7 day bins. The different colored shaded regions correspond to different ZTF bands (r : red, g : green, and i : gray). The solid lines depict the upper limits on the fraction of the time a precursor of the corresponding magnitude would have been detected that are consistent with the ZTF nondetections.

3.5. Precursor Rates

The ZTF precursor rates were calculated following the method in Strotjohann et al. (2021), who studied the frequency of precursors in interacting SNe found by ZTF. Strotjohann et al. (2021) included six of the SNe Ia-CSM presented in this paper in addition to four other SNe Ia-CSM not in this paper (see the Appendix for details) for their search, but they did not find any robust 5σ precursor detections. This nondetection was concluded to be due to the small sample size of SNe Ia-CSM (or that they are more distant) compared to the SN IIn sample, so even if the precursors were as bright or frequent as for SNe IIn, it would be difficult to detect them.

The same search was here carried out for our larger sample by taking the ZTF forced-photometry multiband (g , r , and i) light curves generated by the pipeline outlined in Masci et al. (2019) and stacking them in 1, 3, and 7 day long bins to search for faint outbursts. There were 7389 total available preexplosion epochs for BTS SNe Ia-CSM, the earliest epoch being 1012 days prior to the explosion and the median phase 340 days prior. Hence the results are valid for typical SN Ia-CSM progenitors at about ~ 1 yr before the SN. We did not find any robust 5σ precursor detections. The upper limits for the precursor rates in the different bands are shown in Figure 14, where the solid lines indicate up to what fraction of the time a precursor of a given brightness could have been detected while being consistent with the ZTF nondetections. A precursor of -15 mag could occur as frequently as $\sim 10\%$ of the time given the ZTF nondetections. A continuous search for precursors as more SNe Ia-CSM are found and classified and their sample size increases could yield a detection if the precursors are as frequent and bright as for SNe IIn. The dense and massive CSM around these objects is close enough to have been deposited within decades prior to the SN but the lack of precursors within 1 yr indicates that there is likely no violent event that ejects a lot of mass in that period. Probing for precursors could potentially constrain the progenitor in at least some cases. For example, Soker et al. (2013) predicts using their core-degenerate (CD) model that PTF11kx-like SNe release a significant amount of energy ($\sim 10^{49}$ erg) before explosion over timescales of several years, implying a

precursor 3–7 mag fainter than the SN explosion spread over several years, peaking in the NIR.

4. Discussion

4.1. Fraction of SNe Ia-CSM with Delayed Interaction

The fastest declining SNe in our sample (SNe 2018crl, 2020qzx, and 2020aekp) are also the ones that develop a plateau and show relatively stronger SN Ia-like absorption features in their early spectra. They seem to have a delayed start for the interaction, like PTF11kx, but not as fast of a decline, and thus bridge the gap between PTF11kx and the rest of the strongly interacting SNe Ia-CSM. It remains to be seen how many SNe Ia are weakly interacting where the CSM interaction starts in earnest at timescales of \sim year or more after the explosion. Dubay et al. (2022) constrained the rate of late-onset CSM interaction (similar to that of PTF11kx) to be $\leq 5.1\%$ between 0 and 500 days after discovery by searching for late-time UV excess in GALEX data of 1080 SNe Ia. A similar study in the optical with ZTF data, currently undertaken by J. H. Terwel et al. (2023, in preparation) is searching for faint detections in carefully calibrated forced-photometry light curves (stacked to go fainter). From the current sample, it appears that in addition to SNe Ia-CSM being intrinsically rare, delayed interaction SNe Ia-CSM are even rarer and only constitute about a quarter of all SNe Ia-CSM. This delayed interaction behavior could also be an effect of an asymmetric or clumpy CSM wherein part of the SN ejecta shine through depending on the viewing angle. Observational campaigns that capture the inner boundary of the CSM and the geometry robustly could shed light on the distribution of the inner CSM radius and reveal if it is a continuous distribution or if there are multiple progenitor scenarios within the SN Ia-CSM class.

4.2. Implications for the Progenitors Based on the Observed Mass-loss Rates

From Figure 10, the estimated mass-loss rates from a simple spherical treatment of the CSM and a stationary wind lie between $\sim 10^{-3}$ and $10^{-1} M_{\odot} \text{ yr}^{-1}$ over a period of less than ~ 60 yr before explosion. These give a total mass loss of ~ 0.1 to $\sim 1 M_{\odot}$. Dilday et al. (2012) estimated $\sim 5 M_{\odot}$ of CSM around PTF11kx while Graham et al. (2017) revised it to be $\sim 0.06 M_{\odot}$. Light-curve modeling of SN 1997cy and SN 2002ic by Chugai & Yungelson (2004) resulted in $\sim 5 M_{\odot}$ estimates for both SNe. Inserra et al. (2016) also fit analytical models to some SNe Ia-CSM and found that the CSM masses lie between 0.4 and $4.4 M_{\odot}$. Since from Figure 5, the pseudo-bolometric luminosities of our SNe Ia-CSM lie somewhere between PTF11kx and SNe 1997cy, 2002ic, and 2005gj, with SN 1999E somewhere in the middle, we can say that the total CSM mass in our sample of SN Ia-CSM should also be several solar masses. A WD+AGB star system has typically been suggested for historical SNe Ia-CSM to explain this massive CSM. The WD could either gain mass through Roche Lobe overflow (RLOF) from the companion that drives an optically thick wind (OTW) or merges with the core of the AGB star that then explodes in or soon after the common envelope phase. Meng & Podsiadlowski (2019) model WD+main sequence systems for their common envelope wind (CEW) model and find $\sim 1 M_{\odot}$ CSM around SNe Ia-CSM. Thus, given the large observed CSM mass range, the nature of the companion cannot be solely determined from the total mass lost. High-resolution

spectroscopy that can resolve the narrow unshocked CSM wind velocity is also needed to determine the compactness of the companion.

4.3. Implications for the Progenitor Based on the Observed Volumetric Rate

Robust observed rate estimates for SNe Ia-CSM have been few and far between. Dilday et al. (2010) found one interacting SN Ia (SN 2005gj) in a sample of 79 SNe Ia at $z < 0.15$ in the SDSS-II SN survey, giving a rate of $\sim 1\%$. After the PTF11kx discovery in the PTF survey, the SN Ia-CSM rate was estimated to be $\sim 0.1\%$ (1 in 1000 classified SNe Ia; Dilday et al. 2012) but without spectroscopic completeness determination. S13 identified seven more SNe Ia-CSM from the PTF SN IIn sample, bumping up the estimate to $\sim 0.8\%$. With this sample we have improved the rate estimate, providing a robust value (along with an uncertainty estimate on that value) from an unbiased survey with high spectroscopic completeness up to 18.5 mag. However this rate quite possibly still underestimates the true value for two reasons. The first being possible thermonuclear SNe that are enshrouded so completely by CSM interaction that they are misclassified as SNe IIn in the absence of good early-time data. In the BTS SN IIn sample, we found six SNe IIn to have ambiguous classifications, which could possibly be SNe Ia-CSM and these are described in the Appendix. Including these ambiguous cases in the rate estimation results in a rate upper limit of 0.07%–0.8% for strongly interacting thermonuclear SNe, while excluding them gives an underestimated rate of 0.02%–0.2%.

The second issue with the rates is if there is indeed a continuum of delayed interaction SNe Ia-CSM like PTF11kx, interaction in SNe Ia may present itself hundreds of days later at magnitudes fainter than ZTF’s limit (~ 20.5) resulting in those SNe not being counted when they may be sharing the same progenitor as the rest of the interacting SNe Ia-CSM. Lastly in some rare cases, the SN might appear normal in its light-curve shape and duration (and thus would be missed by the selection criteria used in this paper) but seem to have peculiar narrow H α in its spectrum or bright mid-IR flux (like in the case of SN 2020aaym; Thévenot et al. 2021).

Han & Podsiadlowski (2006) predicted a rate of 0.1%–1% for 02ic-like events for their delayed dynamical instability SD model but could not naturally explain the delayed interaction and multiple CSM shells in PTF11kx (which is relevant for some SNe in our sample). A symbiotic nova-like progenitor was suggested by Dilday et al. (2012) for PTF11kx and they quoted the theoretical rates for the same to lie between 1%–30%; however, their model could not explain the massive CSM. Soker et al. (2013) suggested a CD scenario in which the explosion is set by the violent prompt merger of the core of the giant companion on to the WD and could naturally explain the massive CSM of PTF11kx (Livio & Riess 2003). Soker et al. (2013) estimated the occurrence of such SNe ($M_{\text{core}} + M_{\text{WD}} \gtrsim 2 M_{\odot}$ and $M_{\text{env}} \gtrsim 4 M_{\odot}$) through population synthesis and found it to be 0.002 per 1000 M_{\odot} stars formed. Assuming ~ 1 –2 SNe Ia occur per 1000 M_{\odot} stars formed (Maoz et al. 2012), this corresponds to 0.1%–0.2%, which compares well with our observed rate estimate.

The CEW model by Meng & Podsiadlowski (2019) predicts that the SNe Ia-CSM like objects could arise in the SD common envelope evolution (CEE) scenario when CONE WDs steadily accrete material at the base of the common envelope

without quickly spiraling in due to the driving of a CEW wind ($10\text{--}100\text{ km s}^{-1}$). The WD explodes when it reaches the Chandrasekhar mass ($1.38 M_{\odot}$) and could possibly explode within the common envelope before it is ejected. The CEW model predicts that 25%–40% of the SNe Ia from CONe WD in CEE with a MS companion will show SN Ia-CSM-like properties. Meng & Podsiadlowski (2019) also give the ratio of SNe Ia from CONe WDs to normal SNe Ia from CO WDs to be between 1/9 and 1/5 (considering normal SNe Ia only come from CO WD + MS systems). Combining that with the estimate that roughly 10%–20% of all SNe Ia may come from the SD scenario (Hayden et al. 2010; Bianco et al. 2011), SNe Ia-CSM from CONe WDs according to the CEW model should be 0.28% to 1.6% of all SNe Ia. A spin-down before explosion of the WD (Justham 2011; Di Stefano & Kilic 2012) could also explain the time delay between explosion and interaction.

Soker (2022) estimated the common envelope to explosion delay time distribution (CEEDTD) shortly after the CEE ($t_{\text{CEED}} < 10^4\text{ yr}$) from SN in planetary nebula rates and SN Ia-CSM observed rates to be roughly constant rather than having a t^{-1} dependence; that is, the SN explosion could occur very soon after the CEE as well. Our observed rates are on the lower side compared to these theoretical model estimates but compare well within the observational uncertainties, though the CEW model seems to best account for the overall SNe Ia-CSM properties.

5. Summary

In this paper, we have presented optical and mid-IR photometry, optical spectra, and a detailed analysis of the 12 new SNe Ia-CSM identified in the ZTF BTS, nearly doubling the total number of such objects discussed previously by S13. The properties of the sample extracted in this paper agree very well with the similar analysis conducted in S13, particularly the median EW of $H\beta$ is found to be significantly weaker in SNe Ia-CSM compared with SNe IIn, and consequently the Balmer decrements are ubiquitously higher in SNe Ia-CSM. The brightness of the SNe Ia-CSM in the mid-IR are comparable to SNe IIn, and observations of reduced flux on the red side of the $H\alpha$ wing together with the mid-IR brightness point to the formation of new dust in the cooling postshock gas. The host galaxies of SNe Ia-CSM lie toward late-type galaxies with recent star formation. Unlike SNe IIn, no precursors were found within ~ 1000 days before explosion for SNe Ia-CSM, which could be an observational bias (smaller number of SNe Ia-CSM compared to SNe IIn). We provide a robust rate estimate of 0.02%–0.2% of all SNe Ia being SNe Ia-CSM on account of the BTS survey being unbiased and spectroscopically highly complete. The simple mass-loss rate estimates from the broad $H\alpha$ luminosities of $\sim 10^{-2} M_{\odot}\text{ yr}^{-1}$ are similar to previous estimates from various methods, and indicate several solar masses of CSM around these SNe. The observed rate agrees well within the observational uncertainties with the CEW model by Meng & Podsiadlowski (2019), which can also explain the interaction delay and massive CSM.

There are still many unanswered questions about the nature of the progenitors and if we are accurately identifying all potential members of this class. As ZTF Phase II continues, we are identifying more and more SNe Ia-CSM (interacting with hydrogen-rich and helium-rich CSM) and looking further to the future, if ZTF continues for a Phase III and when LSST survey operations begin, a larger sample would further improve upon

the observed rate calculation. However, individual object studies are as important and detailed spectroscopic and multiwavelength follow up is essential to capture the CSM configuration and mass.

Based on observations obtained with the Samuel Oschin Telescope 48 inch and the 60 inch Telescope at the Palomar Observatory as part of the ZTF project. ZTF is supported by the National Science Foundation under Grants No. AST-1440341 and AST-2034437 and a collaboration including current partners Caltech, IPAC, the Weizmann Institute of Science, the Oskar Klein Center at Stockholm University, the University of Maryland, Deutsches Elektronen-Synchrotron and Humboldt University, the TANGO Consortium of Taiwan, the University of Wisconsin at Milwaukee, Trinity College Dublin, Lawrence Livermore National Laboratories, IN2P3, University of Warwick, Ruhr University Bochum, Northwestern University and former partners the University of Washington, Los Alamos National Laboratories, and Lawrence Berkeley National Laboratories. Operations are conducted by COO, IPAC, and UW. The ZTF forced-photometry service was funded under the Heising-Simons Foundation grant #12540303 (PI: Graham). This work was supported by the GROWTH project (Kasliwal et al. 2019) funded by the National Science Foundation under PIRE grant No. 1545949. The Oskar Klein Centre was funded by the Swedish Research Council. Partially based on observations made with the Nordic Optical Telescope, operated by the Nordic Optical Telescope Scientific Association at the Observatorio del Roque de los Muchachos, La Palma, Spain, of the Instituto de Astrofísica de Canarias. Some of the data presented here were obtained with ALFOSC. Some of the data presented herein were obtained at the W. M. Keck Observatory, which is operated as a scientific partnership among the California Institute of Technology, the University of California, and NASA; the observatory was made possible by the generous financial support of the W. M. Keck Foundation. The SED Machine is based upon work supported by the National Science Foundation under grant No. 1106171. This work has made use of data from the Asteroid Terrestrial-impact Last Alert System (ATLAS) project. The Asteroid Terrestrial-impact Last Alert System (ATLAS) project is primarily funded to search for near earth asteroids through NASA grants NN12AR55G, 80NSSC18K0284, and 80NSSC18K1575; byproducts of the NEO search include images and catalogs from the survey area. The ATLAS science products have been made possible through the contributions of the University of Hawaii Institute for Astronomy, the Queen's University Belfast, the Space Telescope Science Institute, the South African Astronomical Observatory, and The Millennium Institute of Astrophysics (MAS), Chile. This research has made use of the NASA/IPAC Infrared Science Archive, which is funded by the National Aeronautics and Space Administration and operated by the California Institute of Technology. The Liverpool Telescope is operated on the island of La Palma by Liverpool John Moores University in the Spanish Observatorio del Roque de los Muchachos of the Instituto de Astrofísica de Canarias with financial support from the UK Science and Technology Facilities Council.

Y.S. thanks the LSSTC Data Science Fellowship Program, which is funded by LSSTC, NSF Cybertraining grant #1829740, the Brinson Foundation, and the Moore Foundation; her participation in the program has benefited this work.

S.S. acknowledges support from the G.R.E.A.T research environment, funded by *Vetenskapsrådet*, the Swedish Research Council, project number 2016-06012.

This work has been supported by the research project grant “Understanding the Dynamic Universe” funded by the Knut and Alice Wallenberg Foundation under Dnr KAW 2018.0067,

The research of Y.Y. is supported through a Bengier-Winslow-Robertson Fellowship

A.V.F.’s supernova group at UC Berkeley received support from the Christopher R. Redlich Fund and many individual donors.

Fritz (van der Walt et al. 2019; Duev et al. 2019) and GROWTH marshal (Kasliwal et al. 2019) (dynamic collaborative platforms for time-domain astronomy) were used in this work.

Software: LAMBDA (Wright et al. 2016), Prospector (Johnson et al. 2021), pySEDM (Rigault et al. 2019), IRAF (Tody 1986, 1993), pyNOT (<https://github.com/jkrogager/PyNOT>), LPipe (Perley 2019), pypeit (Prochaska et al. 2020), extinction (Barbary 2016), pyraf-dbsp (Bellm & Sesar 2016), FPipe (Fremling et al. 2016), DBSP_DRP (Mandigo-Stoba et al. 2022), ztfquery (Rigault 2018), astropy (Astropy Collaboration et al. 2013, 2018, 2022), matplotlib (Hunter 2007).

Appendix

Ambiguous SN Ia-CSM/II in BTS

To identify potential SNe Ia-CSM hiding in the SN II sample classified by BTS, we rechecked all SNe II classifications (total 142) using the SuperNova Identification (SNID; Blondin & Tonry 2007) software. SNe II spectra were processed through SNID, and any SN having ≥ 3 matches to a SN Ia-CSM in the top 10 matches were manually checked. The SNe having ambiguous classifications are described below.

A.1. SN 2019smj

Discovered by ZTF and reported to TNS by ALERCE (Förster et al. 2021) on 2019 October 13 11:28:42.000, SN 2019smj (ZTF19aceqlxc) was classified as a Type II by BTS at $z = 0.06$. It peaked at an apparent magnitude of 17.1 in the r band (~ -20.1) and then developed a weaker but broader bump. The spectra showed very weak $H\beta$, barely any He I $\lambda 5876$, and no O I $\lambda 7774$ or [O I] lines, but showed some iron-group lines, Ca NIR emission, and [Ca II]. The SNID best matches were to SNe 1997cy and 2005gj. The early spectra from P60/SEDM have some matches to SN 2005gj but are too noisy and of ultra low-resolution to provide a conclusive Ia-CSM classification. From these observations, SN 2019smj is most likely a Type Ia-CSM but given the lack of confirmation we have excluded it from the main sample.

A.2. SN 2018dfa

Discovered and reported to TNS by ATLAS on 2018 July 5 08:51:21.000, SN 2018dfa was classified initially as a Type IIP by BTS but later spectra revealed it to be a Type II in at $z = 0.128$. It peaked at an apparent magnitude of 17.5 in the r band (-20.2) and showed a minor bump before the main peak in the light curve. The spectra showed weak $H\beta$ and He I $\lambda 5876$, and no O I $\lambda 7774$ or [O I] lines. The SNID best matches were to SNe 2002ic and 2005gj along with SNe Ia-norm/91T. The earliest spectra with good S/Ns from P200/DBSP had one match to SN 2005gj but could not provide a robust Ia-CSM

classification. From these observations, SN 2018dfa is most likely a Type Ia-CSM but given the lack of confirmation we have excluded it from the main sample.

A.3. SN 2019vpk

Discovered by ZTF and reported to TNS by ALERCE on 2019 November 25 06:33:38.000, SN 2019vpk was classified as a Type II by BTS at $z = 0.1$. It peaked at an apparent magnitude of ~ 18 in the r band (~ -20.5). The early spectra were too noisy and the only spectrum with a good S/N was obtained with P200/DBSP nearly six weeks after discovery, which showed weak $H\beta$, no clear He I emission, but possibly Si II $\lambda 5958$ emission (which is unlike any other SN Ia-CSM). The SNID top matches were to SN 2005gj but visually did not look entirely convincing, and some matches were also to Type II. We conclude SN 2019vpk does not have enough data for a robust Ia-CSM classification.

A.4. SN 2019wma

Discovered by ZTF and reported to TNS by ALERCE on 2019 December 13 13:35:26.000, SN 2019wma was classified as a Type II by BTS at $z = 0.088$. It peaked at an apparent magnitude of ~ 18.5 in the r band (~ -19.5). The spectra obtained were either from P60/SEDM or LT/SPRAT hence of low resolution and showed weak $H\beta$ and He I emission. The SNID top matches to the earliest SEDM spectrum were to SN 2005gj at the correct redshift but given the lack of intermediate-resolution spectra and the absence of late-time follow up we did not assign a Type Ia-CSM classification to SN 2019wma and excluded it from the main sample.

A.5. SN 2019kep

Discovered and reported to TNS by ATLAS on 2019 July 2 14:13:55.000, SN 2019kep was classified as a Type II by BTS at $z = 0.02388$. It peaked at an apparent magnitude of 18.2 in the r band (-17). Most of the early spectra were too noisy for classification but matched to SN 2005gj. A good S/N P200/DBSP spectrum showed narrow P-Cygni $H\alpha$ with an absorption minimum at $\sim 2500 \text{ km s}^{-1}$, but overall matched to a Type II SN. From these observations, we could not determine a robust classification for SN 2019kep and excluded it from the main sample.

A.6. SN 2018ctj

Discovered and reported to TNS by ZTF on 2018 April 21 08:36:57.000, SN 2018ctj was classified as a Type II by BTS at $z = 0.0378$. It peaked at an apparent magnitude of 18.4 in the r band (-17.8) and was also detected in unWISE data. Only one P60/SEDM spectrum was obtained that matched well to SNe 1997cy and 2005gj. Given the lack of intermediate-resolution spectra this SN remains classified as Type II and was excluded from the main sample.

ORCID iDs

Yashvi Sharma  <https://orcid.org/0000-0003-4531-1745>
 Jesper Sollerman  <https://orcid.org/0000-0003-1546-6615>
 Christoffer Fremling  <https://orcid.org/0000-0002-4223-103X>
 Shrinivas R. Kulkarni  <https://orcid.org/0000-0001-5390-8563>

Kishalay De  <https://orcid.org/0000-0002-8989-0542>
 Ido Irani  <https://orcid.org/0000-0002-7996-8780>
 Steve Schulze  <https://orcid.org/0000-0001-6797-1889>
 Nora Linn Strotjohann  <https://orcid.org/0000-0002-4667-6730>
 Avishay Gal-Yam  <https://orcid.org/0000-0002-3653-5598>
 Kate Maguire  <https://orcid.org/0000-0002-9770-3508>
 Daniel A. Perley  <https://orcid.org/0000-0001-8472-1996>
 Eric C. Bellm  <https://orcid.org/0000-0001-8018-5348>
 Erik C. Kool  <https://orcid.org/0000-0002-7252-3877>
 Thomas G. Brink  <https://orcid.org/0000-0001-5955-2502>
 Rachel Bruch  <https://orcid.org/0000-0001-8208-2473>
 Maxime Deckers  <https://orcid.org/0000-0001-8857-9843>
 Richard Dekany  <https://orcid.org/0000-0002-5884-7867>
 Alison Dugas  <https://orcid.org/0000-0001-7344-0208>
 Alexei V. Filippenko  <https://orcid.org/0000-0003-3460-0103>
 Matthew J. Graham  <https://orcid.org/0000-0002-3168-0139>
 Melissa L. Graham  <https://orcid.org/0000-0002-9154-3136>
 Steven L. Groom  <https://orcid.org/0000-0001-5668-3507>
 Matt Hankins  <https://orcid.org/0000-0001-9315-8437>
 Jacob Jenson  <https://orcid.org/0000-0001-5754-4007>
 Joel P. Johansson  <https://orcid.org/0000-0001-5975-290X>
 Viraj Karambelkar  <https://orcid.org/0000-0003-2758-159X>
 Mansi M. Kasliwal  <https://orcid.org/0000-0002-5619-4938>
 Frank J. Masci  <https://orcid.org/0000-0002-8532-9395>
 Michael S. Medford  <https://orcid.org/0000-0002-7226-0659>
 James D. Neill  <https://orcid.org/0000-0002-0466-1119>
 Guy Nir  <https://orcid.org/0000-0002-7501-5579>
 Reed L. Riddle  <https://orcid.org/0000-0002-0387-370X>
 Mickael Rigault  <https://orcid.org/0000-0002-8121-2560>
 Tassilo Schweyer  <https://orcid.org/0000-0001-8948-3456>
 Jacco H. Terwel  <https://orcid.org/0000-0001-9834-3439>
 Lin Yan  <https://orcid.org/0000-0003-1710-9339>
 Yi Yang (杨轶)  <https://orcid.org/0000-0002-6535-8500>
 Yuhan Yao  <https://orcid.org/0000-0001-6747-8509>

References

- Ahn, C. P., Alexandroff, R., Allende Prieto, C., et al. 2012, *ApJS*, 203, 21
 Aldering, G., Antilogus, P., Bailey, S., et al. 2006, *ApJ*, 650, 510
 Astropy Collaboration, Price-Whelan, A. M., Lim, P. M., et al. 2022, *ApJ*, 935, 167
 Astropy Collaboration, Price-Whelan, A. M., Sipőcz, B. M., et al. 2018, *AJ*, 156, 123
 Astropy Collaboration, Robitaille, T. P., Tollerud, E. J., et al. 2013, *A&A*, 558, A33
 Barbary, K. 2016, extinction v0.3.0, Zenodo, doi:10.5281/zenodo.804967
 Barnsley, R. M., Smith, R. J., & Steele, I. A. 2012, *AN*, 333, 101
 Bellm, E. C., Kulkarni, S. R., Barlow, T., et al. 2019, *PASP*, 131, 068003
 Bellm, E. C., & Sesar, B. 2016, pyraf-dbsp: Reduction pipeline for the Palomar Double Beam Spectrograph, Astrophysics Source Code Library, record ascl:1602.002
 Ben-Ami, S., McLean, I. S., Ramsay, S. K., et al. 2012, *Proc. SPIE*, 8446, 844686
 Benetti, S., Cappellaro, E., Turatto, M., et al. 2006, *ApJL*, 653, L129
 Bianco, F. B., Howell, D. A., Sullivan, M., et al. 2011, *ApJ*, 741, 20
 Blagorodnova, N., Neill, J. D., Walters, R., et al. 2018, *PASP*, 130, 035003
 Blondin, S., Prieto, J. L., Patat, F., et al. 2009, *ApJ*, 693, 207
 Blondin, S., & Tonry, J. L. 2007, *ApJ*, 666, 1024
 Bloom, J. S., Kasen, D., Shen, K. J., et al. 2011, *ApJL*, 744, L17
 Brown, P. J., Dawson, K. S., de Pasquale, M., et al. 2012, *ApJ*, 753, 22
 Byler, N., Dalcanton, J. J., Conroy, C., & Johnson, B. D. 2017, *ApJ*, 840, 44
 Calzetti, D., Armus, L., Bohlin, R. C., et al. 2000, *ApJ*, 533, 682
 Cenko, S. B., Fox, D. B., Moon, D.-S., et al. 2006, *PASP*, 118, 1396
 Chabrier, G. 2003, *PASP*, 115, 763
 Chambers, K. C., Magnier, E. A., Metcalfe, N., et al. 2016, arXiv:1612.05560
 Chugai, N. N. 1991, *MNRAS*, 250, 513
 Chugai, N. N. 2009, *MNRAS*, 400, 866
 Chugai, N. N., Chevalier, R. A., & Lundqvist, P. 2004, *MNRAS*, 355, 627
 Chugai, N. N., & Danziger, I. J. 1994, *MNRAS*, 268, 173
 Chugai, N. N., & Yungelson, L. R. 2004, *AstL*, 30, 65
 Clark, P., Maguire, K., Bulla, M., et al. 2021, *MNRAS*, 507, 4367
 De, K., Hankins, M. J., Kasliwal, M. M., et al. 2020, *PASP*, 132, 025001
 Dekany, R., Smith, R. M., Riddle, R., et al. 2020, *PASP*, 132, 038001
 Deng, J., Kawabata, K. S., Ohyama, Y., et al. 2004, *ApJL*, 605, L37
 Dhawan, S., Goobar, A., Smith, M., et al. 2022, *MNRAS*, 510, 2228
 Di Stefano, R., & Kilic, M. 2012, *ApJ*, 759, 56
 Dilday, B., Howell, D. A., Cenko, S. B., et al. 2012, *Sci*, 337, 942
 Dilday, B., Smith, M., Bassett, B., et al. 2010, *ApJ*, 713, 1026
 Dubay, L. O., Tucker, M. A., Do, A., Shappee, B. J., & Anand, G. S. 2022, *ApJ*, 926, 98
 Duev, D. A., Mahabal, A., Masci, F. J., et al. 2019, *MNRAS*, 489, 3582
 Filippenko, A. V. 1997, *ARA&A*, 35, 309
 Filippenko, A. V., Li, W. D., & Leonard, D. C. 1999, *IAU Circ.*, 7108, 2
 Filippenko, A. V., Richmond, M. W., Matheson, T., et al. 1992, *ApJL*, 384, L15
 Fitzpatrick, E. L. 1999, *PASP*, 111, 63
 Foley, R. J., Smith, N., Ganeshalingam, M., et al. 2007, *ApJL*, 657, L105
 Ford, C. H., Herbst, W., Richmond, M. W., et al. 1993, *AJ*, 106, 1101
 Förster, F., Cabrera-Vives, G., Castillo-Navarrete, E., et al. 2021, *AJ*, 161, 242
 Fox, O. D., Chevalier, R. A., Skrutskie, M. F., et al. 2011, *ApJ*, 741, 7
 Fox, O. D., Silverman, J. M., Filippenko, A. V., et al. 2015, *MNRAS*, 447, 772
 Fremling, C., Miller, A. A., Sharma, Y., et al. 2020, *ApJ*, 895, 32
 Fremling, C., Sollerman, J., Taddia, F., et al. 2016, *A&A*, 593, A68
 Gal-Yam, A., Bruch, R., Schulze, S., et al. 2022, *Natur*, 601, 201
 Gal-Yam, A., & Leonard, D. C. 2009, *Natur*, 458, 865
 Gal-Yam, A., Leonard, D. C., Fox, D. B., et al. 2007, *ApJ*, 656, 372
 Gal-Yam, A., Yaron, O., Pastorello, A., et al. 2021, *TNSAN*, 76, 1
 Germany, L. M., Reiss, D. J., Sadler, E. M., Schmidt, B. P., & Stubbs, C. W. 2000, *ApJ*, 533, 320
 Graham, M. J., Kulkarni, S. R., Bellm, E. C., et al. 2019, *PASP*, 131, 078001
 Graham, M. L., Fremling, C., Perley, D. A., et al. 2022, *MNRAS*, 511, 241
 Graham, M. L., Harris, C. E., Fox, O. D., et al. 2017, *ApJ*, 843, 102
 Guillochon, J., Parrent, J., Kelley, L. Z., & Margutti, R. 2017, *ApJ*, 835, 64
 Hamuy, M., Phillips, M. M., Suntzeff, N. B., et al. 2003, *Natur*, 424, 651
 Han, Z., & Podsiadlowski, P. 2006, *MNRAS*, 368, 1095
 Hayden, B. T., Garnavich, P. M., Kasen, D., et al. 2010, *ApJ*, 722, 1691
 Hodgkin, S. T., Harrison, D. L., Breedt, E., et al. 2021, *A&A*, 652, A76
 Hosseinzadeh, G., Arcavi, I., Valenti, S., et al. 2017, *ApJ*, 836, 158
 Hunter, J. D. 2007, *CSE*, 9, 90
 Iben, I., Jr., & Tutukov, A. V. 1984, *ApJS*, 54, 335
 Inserra, C., Fraser, M., Smartt, S. J., et al. 2016, *MNRAS*, 459, 2721
 Inserra, C., Smartt, S. J., Scalzo, R., et al. 2014, *MNRAS*, 437, L51
 Irani, I., Prentice, S. J., Schulze, S., et al. 2022, *ApJ*, 927, 10
 IRSA 2022, *Zwicky Transient Facility Image Service, IPAC*,
 Johnson, B. D., Leja, J., Conroy, C., & Speagle, J. S. 2021, *ApJS*, 254, 22
 Justham, S. 2011, *ApJL*, 730, L34
 Kasliwal, M. M., Cannella, C., Bagdasaryan, A., et al. 2019, *PASP*, 131, 038003
 Kiewe, M., Gal-Yam, A., Arcavi, I., et al. 2012, *ApJ*, 744, 10
 Kochanek, C. S., Shappee, B. J., Stanek, K. Z., et al. 2017, *PASP*, 129, 104502
 Kool, E., Johansson, J., Sollerman, J., et al. 2022, arXiv:2210.07725
 Kotak, R., & Meikle, W. P. S. 2005, in ASP Conf. Ser. 342, 1604-2004: Supernovae as Cosmological Lighthouses, ed. M. Turatto et al. (San Francisco, CA: ASP), 264
 Lang, D. 2014a, *AJ*, 147, 108
 Lang, D. 2014b, *AJ*, 147, 108
 Leloudas, G., Hsiao, E. Y., Johansson, J., et al. 2015, *A&A*, 574, A61
 Li, W., Bloom, J. S., Podsiadlowski, P., et al. 2011, *Natur*, 480, 348
 Lintott, C., Schwawinski, K., Bamford, S., et al. 2011, *MNRAS*, 410, 166
 Livio, M., & Riess, A. G. 2003, *ApJL*, 594, L93
 Maguire, K., Sullivan, M., Patat, F., et al. 2013, *MNRAS*, 436, 222
 Mainzer, A., Bauer, J., Cutri, R. M., et al. 2014, *ApJ*, 792, 30
 Mandigo-Stoba, M. S., Fremling, C., & Kasliwal, M. M. 2022, *JOSS*, 7, 3612
 Maoz, D., Mannucci, F., & Brandt, T. D. 2012, *MNRAS*, 426, 3282
 Martin, D. C., Fanson, J., Schiminovich, D., et al. 2005, *ApJL*, 619, L1
 Masci, F. J., Laher, R. R., Rusholme, B., et al. 2019, *PASP*, 131, 018003
 Meisner, A. M., Lang, D., & Schlegel, D. J. 2018, *AJ*, 156, 69
 Meng, X., & Podsiadlowski, P. 2019, in IAU Proc. 343, Why Galaxies Care About AGB Stars: A Continuing Challenge through Cosmic Time (Cambridge: Cambridge Univ. Press), 470
 Miller, A. A., Yao, Y., Bulla, M., et al. 2020, *ApJ*, 902, 47

- Miller, J., & Stone, R. 1987, The CCD Cassegrain Spectrograph at the Shane Reflector Technical Rep.No. 48 Lick Observatory
- Nicholls, B., & Dong, S. 2018, TNSCR208-11441
- Nordin, J., Brinnel, V., van Santen, J., et al. 2019, *A&A*, **631**, A147
- Nugent, P. E., Sullivan, M., Cenko, S. B., et al. 2011, *Natur*, **480**, 344
- Oke, J. B., Cohen, J. G., Carr, M., et al. 1995, *PASP*, **107**, 375
- Oke, J. B., & Gunn, J. E. 1982, *PASP*, **94**, 586
- Pastorello, A., Mattila, S., Zampieri, L., et al. 2008, *MNRAS*, **389**, 113
- Patat, F., Chandra, P., Chevalier, R., et al. 2007, *Sci*, **317**, 924
- Payne, A. V., Tucker, M. A., Do, A., Shappee, B. J., & Huber, M. E. 2019, TNSCR, 2019-343, 1
- Pedregosa, F., Varoquaux, G., Gramfort, A., et al. 2011, *JMLR*, **12**, 2825
- Pellegrino, C., Howell, D. A., Terreran, G., et al. 2022, *ApJ*, **938**, 73
- Perley, D. A. 2019, *PASP*, **131**, 084503
- Perley, D. A., Fremling, C., Sollerman, J., et al. 2020, *ApJ*, **904**, 35
- Perley, D. A., Sollerman, J., Schulze, S., et al. 2022, *ApJ*, **927**, 180
- Piasek, A. S., Steele, I. A., Bates, S. D., et al. 2014, *Proc. SPIE*, **9147**, 91478H
- Prentice, S., Maguire, K., Magee, M. R., & Deckers, M. 2020, TNSCR, 2020-2285, 1
- Prieto, J. L., Garnavich, P. M., Phillips, M. M., et al. 2007, arXiv:0706.4088
- Prochaska, J., Hennawi, J., Westfall, K., et al. 2020, *JOSS*, **5**, 2308
- Reguitti, A. 2020, TNSCR, 2020-3825, 1
- Rigault, M. 2018, ztfquery, a python tool to access ZTF data, vdoi, Zenodo, doi:10.5281/zenodo.1345222
- Rigault, M., Neill, J. D., Blagorodnova, N., et al. 2019, *A&A*, **627**, A115
- Salamanca, I., Cid-Fernandes, R., Tenorio-Tagle, G., et al. 1998, *MNRAS*, **300**, L17
- Schlafly, E. F., & Finkbeiner, D. P. 2011, *ApJ*, **737**, 103
- Schlegel, E. M. 1990, *MNRAS*, **244**, 269
- Schmidt, B. P., Kirshner, R. P., Leibundgut, B., et al. 1994, *ApJL*, **434**, L19
- Schulze, S., Yaron, O., Sollerman, J., et al. 2021, *ApJS*, **255**, 29
- Shappee, B., Prieto, J., Stanek, K. Z., et al. 2014, AAS Meeting, **223**, 236.03
- Silverman, J. M., Nugent, P. E., Gal-Yam, A., et al. 2013, *ApJ*, **207**, 3
- Silverman, J. M., Nugent, P. E., Gal-Yam, A., et al. 2013, *ApJ*, **772**, 125
- Simon, J. D., Gal-Yam, A., Gnat, O., et al. 2009, *ApJ*, **702**, 1157
- Skrutskie, M. F., Cutri, R. M., Stiening, R., et al. 2006, *AJ*, **131**, 1163
- Smartt, S. J., Valenti, S., Fraser, M., et al. 2015, *A&A*, **579**, A40
- Smith, K. W., Smartt, S. J., Young, D. R., et al. 2020, *PASP*, **132**, 085002
- Smith, N. 2014, *ARA&A*, **52**, 487
- Smith, N., Chornock, R., Li, W., et al. 2008, *ApJ*, **686**, 467
- Soker, N. 2022, *RAA*, **22**, 035025
- Soker, N., Kashi, A., García-Berro, E., Torres, S., & Camacho, J. 2013, *MNRAS*, **431**, 1541
- Soraisam, M., Matheson, T., & Lee, C.-H. 2021, *RNAAS*, **5**, 62
- Soumagnac, M. T., & Ofek, E. O. 2018, *PASP*, **130**, 075002
- Steele, I. A., Smith, R. J., Rees, P. C., et al. 2004, *Proc. SPIE*, **5489**, 679
- Stein, R., Callis, E., Kostrzewa-rutkowska, Z., Fraser, M., & Yaron, O. 2018, TNSCR, 2018-1168, 1
- Sternberg, A., Gal-Yam, A., Simon, J. D., et al. 2011, *Sci*, **333**, 856
- Strothjohann, N. L., Ofek, E. O., Gal-Yam, A., et al. 2021, *ApJ*, **907**, 99
- Taddia, F., Stritzinger, M. D., Sollerman, J., et al. 2013, *A&A*, **555**, A10
- Taggart, K. 2020, PhD thesis, Liverpool John Moores Univ., <http://researchonline.ljmu.ac.uk/id/eprint/14104/>
- Taubenberger, S., Kromer, M., Hachinger, S., et al. 2013, *MNRAS*, **432**, 3117
- Thévenot, M., Kabatnik, M., & Gantier, J. M. 2021, TNSAN, **212**, 1
- Tody, D. 1986, *Proc. SPIE*, **627**, 733
- Tody, D. 1993, in ASP Conf. Ser. 52, Astronomical Data Analysis Software and Systems II, ed. R. J. Hanisch, R. J. V. Brissenden, & J. Barnes (San Francisco, CA: ASP), 173
- Tonry, J. L., Denneau, L., Heinze, A. N., et al. 2018, *PASP*, **130**, 064505
- Tucker, M. A., Huber, M., Shappee, B. J., et al. 2018, ATel, **11444**, 1
- van der Walt, S. J., Crellin-Quick, A., & Bloom, J. S. 2019, *JOSS*, **4**, 1247
- Wang, L., Baade, D., Hflich, P., et al. 2004, *ApJL*, **604**, L53
- Webbink, R. F. 1984, *ApJ*, **277**, 355
- Whelan, J., & Iben, I., Jr. 1973, *ApJ*, **186**, 1007
- Wood-Vasey, W. M., Wang, L., & Aldering, G. 2004, *ApJ*, **616**, 339
- Wright, A. H., Robotham, A. S. G., Bourne, N., et al. 2016, *MNRAS*, **460**, 765
- Wright, E. L., Eisenhardt, P. R. M., Mainzer, A. K., et al. 2010, *AJ*, **140**, 1868
- Xu, Y., McCray, R., Oliva, E., & Randich, S. 1992, *ApJ*, **386**, 181
- Yang, Y., Baade, D., Hoefflich, P., et al. 2022, *MNRAS*, **519**, 1618
- Yao, Y., Miller, A. A., Kulkarni, S. R., et al. 2019, *ApJ*, **886**, 152
- Yaron, O., & Gal-Yam, A. 2012, *PASP*, **124**, 668
- Zackay, B., Ofek, E. O., & Gal-Yam, A. 2016, *ApJ*, **830**, 27